HIGH-SENSITIVITY IMAGING OF MAGNETIC FIELDS FROM CARDIAC APEX ACTION POTENTIAL PROPAGATION USING SUPERCONDUCTING QUANTUM INTERFERENCE DEVICE (SQUID) MICROSCOPY

By

Krista Kay M^{c}Bride

Dissertation

Submitted to the Faculty of the

Graduate School of Vanderbilt University

in partial fulfillment of the requirements

for the degree of

DOCTOR OF PHILOSOPHY

in

Physics

August, 2008

Nashville, Tennessee

Approved:

Professor Franz J. Baudenbacher

Professor Alan Bradshaw

Professor Sait A. Umar

Professor Michael I. Miga

Professor John P. Wikswo

To my loving husband James

and

our wonderful families and friends

ACKNOWLEDGEMENTS

This work would not have been possible without the financial support from NIH and the McMinn scholarship.

I would like to thank everyone that gave me much needed support throughout my graduate career. Thanks to my committee members for their guidance and support along the path of earning my Ph.D.

My families, friends and husband deserve great thanks. I love them always! Special thanks to my husband Dr. James McBride. He has been with me through it all! He is my best friend and true love. I couldn't ask for anything more!

TABLE OF CONTENTS

LIST OF TABLES

LIST OF FIGURES

CHAPTER I

INTRODUCTION

Objectives

The more we understand about how the heart functions electrically the better our ability to diagnose and treat patients. Our research group at Vanderbilt has emphasized the study and analysis of how action currents flow throughout the heart, using techniques such as epifluorescent imaging, Superconducting Quantum Interference Device (SQUID) magnetometry, and bidomain modeling. Currently the propagation of action currents and action potentials through cardiac tissue is not well understood, due to the complicated anisotropies and heterogeneities that occur in myocardium.[1,2] These anisotropies and heterogeneities determine the spread of the action currents, which affect the initiation and propagation of action potentials in the heart.[3-6] Many experiments have been conducted on the heart, but there is still more to learn by studying the effects of cardiac tissue structure on the propagation of action currents.

The objective of this research project is to study the action currents of the heart associated with stimulation at the apex using SQUID microscopy and epifluorescent imaging. A coexisting project has been the optimization of the SQUID microscope by implementing monolithic SQUID chips, which have low noise and high sensitivity, into the microscope.

SQUID microscopes have been used in many different areas of research, including biological studies, geomagnetic characterization, and nondestructive testing. In

fact, these three different areas are currently under investigation at Vanderbilt using SQUID microscopes. The Living State Physics (LSP) group at Vanderbilt has developed some of the best low-temperature SQUID microscopes in the world. Depending on the investigation, the SQUID microscope could have a high sensitivity, as good as 300 $fT/Hz^{1/2}$, [1,7-9] or high spatial resolution, to approximately 100 μm.[10-12]

The apex, the lowest point, of the heart is important to examine due to its complex spiral architecture.[13-15] The fiber orientation plays an important role in the development and spread of action currents and magnetic fields during stimulation at the apex. This spiral construction produces both radial and circular currents, potentially contain electrically silent components.[16] By measuring the magnetic fields from the action currents, as well as making transmembrane potential measurements, complementary information may be obtained. In determining both the magnetocardiogram (MCG) and electrocardiogram (ECG), more information might be found that could advance the medical field in the determination of the health condition of a patient's heart.[17,18]

Using an LSP SQUID microscope, magnetic fields of an isolated rabbit heart, which generates weak fields on the order of a picoTesla,[19] can be imaged. The transmembrane potential and magnetic fields associated with the action currents can be imaged using a combination of optical fluorescence techniques and noninvasive SQUID microscopy, respectively.

A coexisting project working with SQUID magnetometers is optimizing this instrument in order to expand its experimental measurement capabilities. To begin with, we have designed and developed a flexure-bearing and lever mechanism system that controls the distance between the SQUID sensor and the sample. This allows better

position precision to minimize the distance between the magnetic sensor and sample.[12] In addition, monolithic SQUID sensors are being optimized by using a set of known intrinsic equations.[19] Also, a process has been formulated to characterize the SQUID chips, mount the SQUID chips into the SQUID Dewar system, and measure their noise.[12]

The following chapters present the design and development of the SQUID microscope, describe our optical mapping technique, and discuss in depth the application of optical mapping and SQUID microscopy to the apex of the heart.

CHAPTER II

LOW TEMPERATURE, MINATURE SENSOR, DC-SQUID MICROSCOPY

Background

The low-temperature SQUID microscope at Vanderbilt can scan samples that are at room temperature and image magnetic fields of around 300 fT magnitude.[12] Because the SQUID has such high sensitivity,[12,20-22] weak magnetic fields, such as those generated by electrical activity at the apex of the heart, can be detected (see Figure 1).[19]

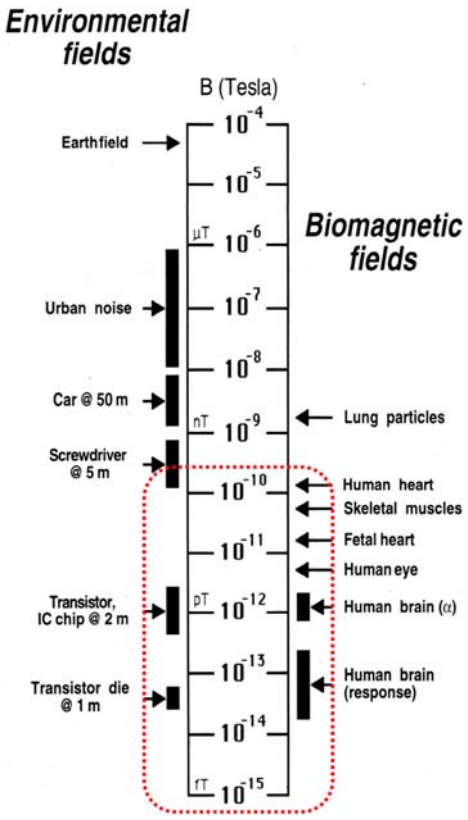

Figure 1 The magnetic field ranges for different environmental and biomagnetic fields.[19]

A SQUID is basically a flux-to-voltage transducer. It detects the flux due to the magnetic field threading the SQUID loop and then transforms the flux into a voltage, as shown in Figure 2 and by the equation

$$\Phi = \int \vec{B} \cdot d\vec{A} \tag{1}$$

where Φ is the flux and B is the magnetic field detected in surface area A.[19,21,23,24]

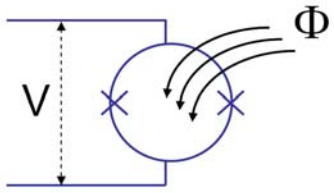

Figure 2 A flux-to-voltage transducer.[25]

The DC-SQUID (Figure 3), which is used in the Vanderbilt microscopes, consists of a circuit that has two Josephson junctions in parallel (represented as X's in Figure 3) with a resistor placed in parallel to each junction. The self-capacitance of the Josephson junction is represented by a capacitor that is in parallel to both the resistor and the junction.[19,26-31]

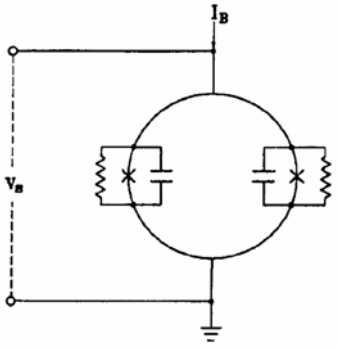

Figure 3 The DC SQUID.[19]

Two key superconductive properties allow the SQUID to perform as a flux-to-voltage transducer. First, flux in a superconducting loop is quantized in units of flux

quantum. This is due to the Meissner effect, where supercurrents are formed in a superconducting ring. These supercurrents keep the magnetic field from entering the ring by opposing any change in magnetic flux. Once the supercurrents cannot support the change in field, the magnetic flux is allowed to enter the ring in integer units of one flux quantum. Therefore, the flux entering the ring is quantized.[19,26,28,29,32-36] The Josephson effect is the second superconductive property used in SQUID operation. A Josephson junction consists of an insulator situated between two superconductors, as seen in Figure 4. When current tunnels through the insulator from one superconductor to another, a phase shift occurs in the wave equation describing this current. This phase shift leads to the Josephson junction equations for the voltage and current across the junction.[19,26,28-30,33,37,38]

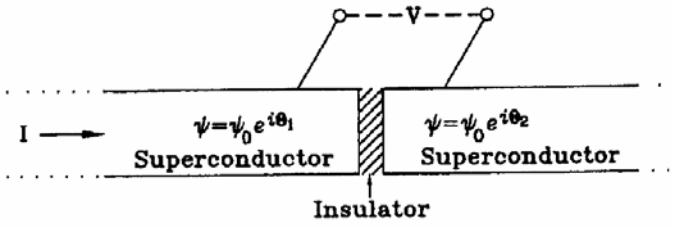

Figure 4 The Josephson Junction[19].

When a DC current that is under the critical current, *Ic,* is pushed through the Josephson junction, a phase shift occurs in the current: the critical current is the maximum current that can be carried across the junction before a voltage drop occurs across the superconductor. This phase shift in current is given by

$$I = I_c \sin\delta \tag{2}$$

$$\delta = \theta_1 - \theta_2 \tag{3}$$

where the δ is the phase change, θ_1-θ_2. If the current sent through the Josephson junction is above the critical threshold, the current will oscillate with a phase difference that increases in time. This is shown as

$$V = \frac{\hbar}{2e}\frac{\partial \delta}{\partial t} \tag{4}$$

where V is the voltage and Φ_0 is one flux quantum ($\Phi_0 = (h/(2e) = 2.07\text{x}10^{-15}$ Wb).[19]

Two characteristic graphs can be made from the DC SQUID under the above conditions, a plot of voltage versus current and one of voltage versus applied flux. The IV curve shown in Figure 5 is obtained by applying a time-varying current to the SQUID. If the current falls below the critical current, the voltage remains at zero and the SQUID remains superconducting. However, once the critical current value is reached, a jump occurs to a nonzero voltage at which the SQUID is no longer superconductive. If a small flux that is less than $\Phi_0/2$ is applied to the SQUID, an opposing circulating current is created that superimposes onto the constant bias current. This changes the critical current where the voltage drop occurs, *i.e.*, the critical current depends on how much magnetic field is applied. This can be seen in Figure 5, where the critical current changes for $\Phi_0 = n\Phi_0$ and $(n+1/2)\Phi_0$.[19,26,28,29,33]

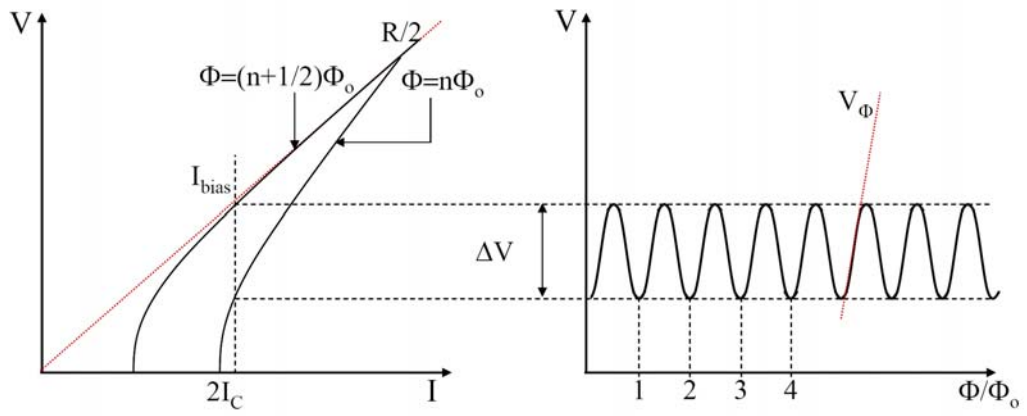

Figure 5 Characteristics of the SQUID. The I-V curve and the V-Phi Curve.[25]

If a constant bias current is applied that is greater than $2I_C$, the voltage will oscillate with a period of one flux quantum between the $n\Phi_0$ and $(n+1/2)\Phi_0$ states if the external magnetic field is much larger. This produces a sinusoidal pattern of voltage versus flux that has a minimum and maximum voltage, as shown in Figure 5. The maxima in the modulation voltage can then be measured by measuring the difference peak to peak voltage. The best performance of the SQUID can be obtained when it is operated at the steepest slope of the voltage versus applied flux curve as a null detector utilizing the flux-lock loop. It is then that the SQUID can detect very small external magnetic fields and produce output voltages. The SQUID acts as a flux-to-voltage transducer.[19,26,28,29,33]

An important consideration in SQUID performance is the elimination of hysteresis in the current-voltage characteristics, which occurs when one value of current could produce multiple voltage values (Figure 6). If hysteresis exists, the SQUID will exhibit high flux noise. Optimally, the Josephson junctions must be shunted with a proper resistance to eliminate this problem.[10,19,39]

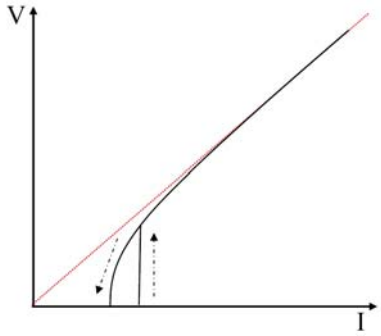

Figure 6 Hysteresis in I-V.[25]

By placing the SQUID in a flux-locked-loop (FLL) configuration (Figure 7) with flux modulation, the SQUID measurement system becomes a linearized null detector. The output voltage from the SQUID is coupled into the FLL. The coupled SQUID signal is mixed with a signal sent from the oscillator. The signals are both multiplied and then integrated. If the magnetic flux in the SQUID is $n\Phi_0$ (Figure 7a), then the integrated signal is a rectified sine wave of the input signal (containing a frequency of 2 times the modulation frequency), and the lock-in amplifier will send output of zero. However, if the flux in the SQUID is $(n+1/4)\Phi_0$ (Figure 7b), then the output from the FLL is maximum and negative the change in flux. This signal is sent back via a feedback resistor and a feedback loop to the SQUID sensor nulling the SQUID. This system – the SQUID sensor in the FLL circuit – produces an extremely sensitive flux-to-voltage transducer that can detect flux from magnetic fields of much less than one flux quantum accuracy.[23,24,28,29,31,33,40]

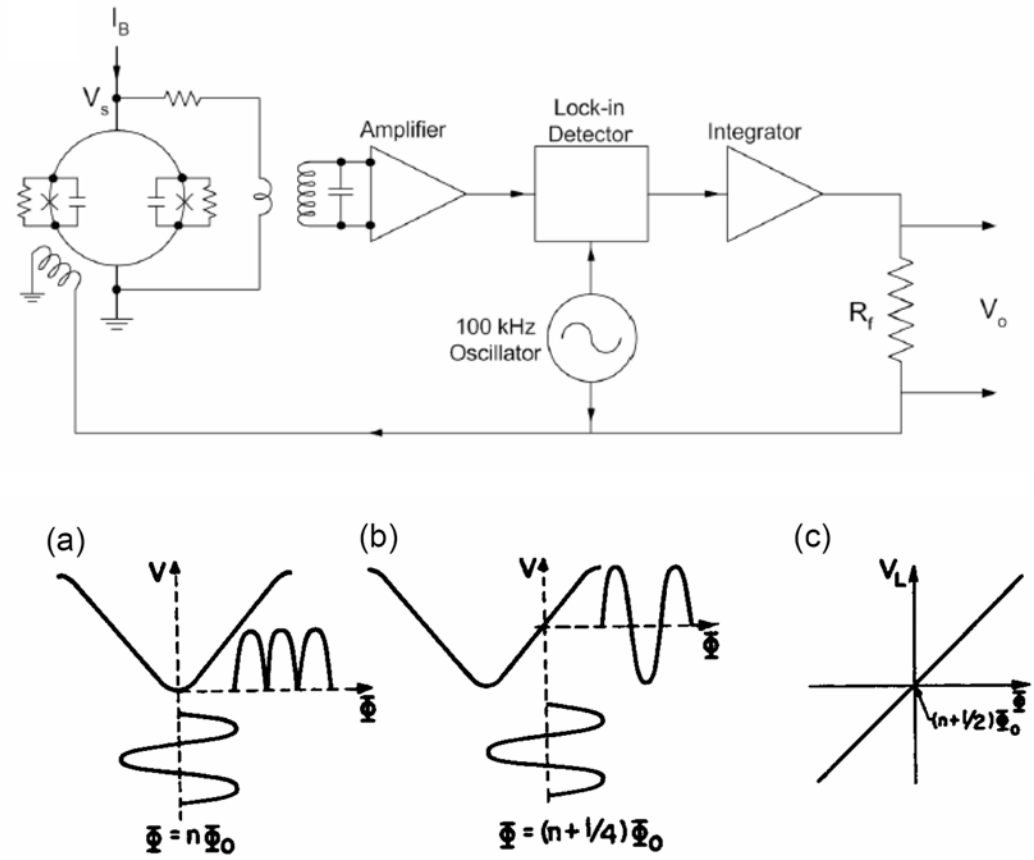

Figure 7 The flux-locked loop. a) $\Phi = n\Phi_0$ b) $\Phi = (2+1/4)\Phi_0$ c) The linearized signal, FLL output V_L versus SQUID input Φ.[19]

SQUID sensor design

Because the SQUID sensor only works when it is superconducting, it must be housed inside a Dewar that provides the necessary cryogenic temperatures and thermal insulation to operate the low temperature SQUID. The Dewar system, shown in Figure 8 and described in more detail in Chapter 4,[12] is the major component of the SQUID microscope that allows the SQUID to make magnetic measurements at close proximity to room temperature samples. Not only must the SQUID sensor be kept cold, but the Dewar system must keep the SQUID superconducting, shield it from outside thermal and electromagnetic radiation sources, and control the pickup coil-to-sample distance (Figure 9).

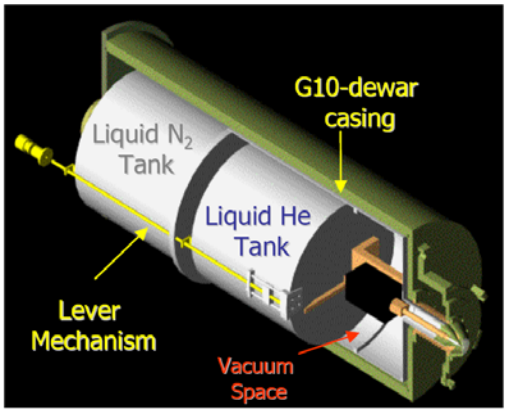

Figure 8 The SQUID Dewar system.[12]

The SQUID Dewar is kept under vacuum with a pressure on the order of 10^{-5} Pa. It is cooled by thermally linked nitrogen and helium reservoirs. The nitrogen cools the inside of the SQUID microscope to about 77 K to minimize radiation load and decrease the helium boil-off (loss of 1.4L/day). The helium reservoir cools the inside of the SQUID microscope even further, to 4.2 K. The inside of the Dewar and the sides of the liquid nitrogen and helium tanks and thermal shields are covered with super-insulation (aluminized Mylar wrapping), decreasing the radiation load and reducing the evaporation of the cooling liquids.[1,7,25] A cryopump that uses activated charcoal is thermally linked to the helium tank and helps maintain an even better insulated vacuum for longer periods of time.[41,42] An aluminum thermal shield attached to the helium Dewar surrounds the open space where the SQUID sensor is located and further cools the SQUID. The bottom of the aluminum thermal shield is formed by an aluminum disk that supports a cylindrical aluminum cylinder, termed a "stovepipe" that is capped with a G-10 cone, both of which are wrapped with aluminized Mylar. This assembly reduces the radiative loading to the SQUID and/or pickup coil. A 25 μm sapphire window separates the liquid helium temperature SQUID sensor in the vacuum space from the room temperature sample.

Sapphire is used because it is transparent, allowing easy centering of the SQUID sensor; yet strong, so that it can support the difference between the vacuum and atmospheric pressure; and is an electric insulator which has negligible Johnson noise.[1,7,12,43]

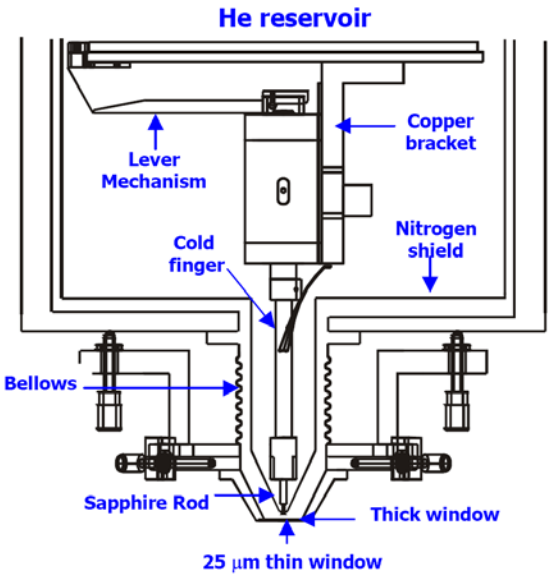

Figure 9 The SQUID Dewar tail.[12]

One of the great accomplishments of our SQUID microscope design is the lever mechanism that controls the sensor to sample distance.[1,12] This is especially important in achieving high spatial resolution in the imaged magnetic fields. If high spatial resolution is desired, a smaller sensor and smaller distance from the sample are needed.[12,44-46] Of course, there is always a trade-off with spatial resolution and field sensitivity. The sensor needs to be large enough to achieve the desired field sensitivity, which depends on the diameter of the sensor.[12,19,27,30,47-49] Another consideration is the magnetic field, which falls off as the distance increases from the sample. Therefore, the sensor needs to be as close as possible to the sample, as shown in Figure 10. For example, the magnetic field of a current-carrying wire falls off as $1/r$, while the magnetic field falls off by $1/r^2$ for a current dipole sources immersed in a conducting medium and $1/r^3$ for a magnetic dipole,

where *r* is distance from the sample.[19,30,48] The smallest distance that we have been able to document with our lever mechanism is approximately 100 μm between the sensor and sample.[12]

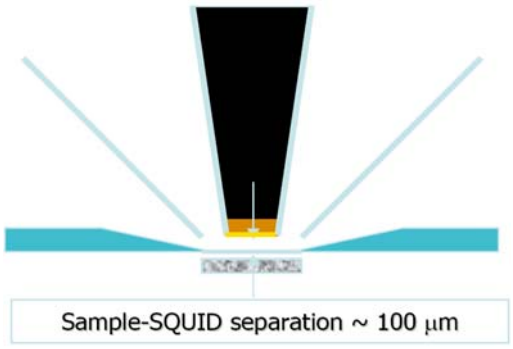

Figure 10 The sensor to sample separation distance. The SQUID chip is in gold.[25]

The lever mechanism design that controls the SQUID sensor's height is shown in Figure 9. It is thermally linked onto the bottom of the helium tank with Apiezon grease (a thermal paste). The lever mechanism consists of a flexure bearing[50,51] mechanism attached to a lever arm that is controlled from outside the SQUID Dewar through a rotational feed-through. This lever mechanism is used to adjust the pickup coil close to the 25 μm sapphire window with an accuracy of a few microns.[1,12]

Another positioning device that moves the sapphire window closer to the SQUID sensor consists of a bellow mechanism, which is attached to the sapphire window's cone. The bellows can be compressed by adjusting the three micrometer screws, which are also used to center the window to the SQUID sensor, as shown in Figure 9.[1,7,12]

Depending on the needs of different research projects, the SQUID microscopes can be modified in order to accomplish either high spatial resolution (around 100 μm) using the monolithic configuration or high sensitivity (around 300 fT) using the pickup coil configuration (due to the trade-off between spatial resolution and field sensitivity).

For better spatial resolution, the SQUID sensor or coil should be as small as possible,[12,44-46] whereas for more sensitivity, the SQUID sensor or coil should be as big as possible.[12,19,27,30,47-49] (Of course, there are limits in the designs due to functionality and noise, and these will be described later.)

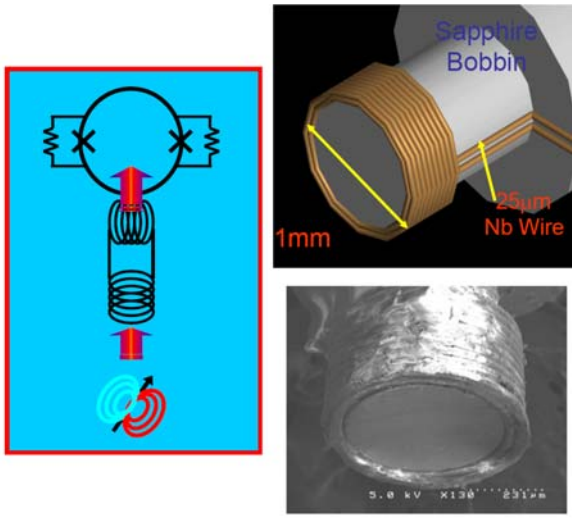

Figure 11 The pickup coil configuration SQUID design.[25]

We used the SQUID and pickup coil configuration[28,29,33] shown in Figure 11 to measure the magnetic field of the heart and apex. The pickup coil detects the magnetic flux and directly couples the signal to a flux transformer circuit of a commercial low-temperature SQUID (Quantum Design). The pickup coil consists of a 25 μm diameter niobium wire that becomes superconducting at low temperatures. This wire is hand wound around the tip of a sapphire bobbin with a diameter of either 250 or 500 μm. The coil is wrapped in aluminized Mylar for protection from radiation. The sapphire bobbin is mounted inside a copper cold finger and is thermally linked by application of Apiezon grease. The cold finger attaches to the collet of the lever mechanism. The cold finger is thermally linked through copper mesh wires, lightly coated with Apiezon grease on the

ends, which attach to the lever mechanism's copper bracket. The ends of the coil are threaded through lead tubing, which serves as both a radiation and superconducting magnetic shield, and are then attached to the transformer on a commercially made SQUID sensor (Quantum Dynamics, San Diego). The SQUID sensor is mounted in a niobium canister which attaches to the side of the copper bracket of the lever mechanism. The positioning of the pickup coil can then be controlled by the lever mechanism.[1,7,26]

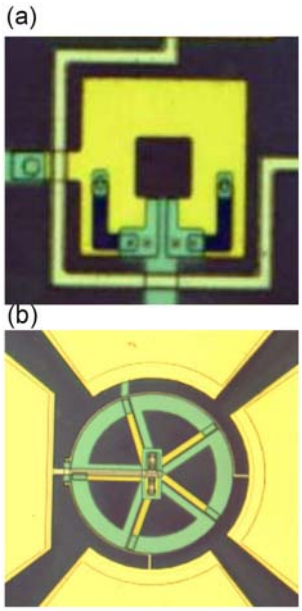

Figure 12 The monolithic SQUID chip designs. a) the bare design, b) the multiloop design.

Another SQUID design we used is the monolithic niobium, thin-film lithographic SQUID sensor,[27,30,52,53] in our case manufactured by HYPRES, Inc., which does not use a pickup coil. The monolithic SQUID directly detects the magnetic flux itself (Figure 12). The SQUID sensor is mounted on the tip of the sapphire bobbin (Figure 13). Small, thin wires are attached to SQUID contact pads by silver paint. Stycast epoxy (Lakeshore) is used to hold the SQUID and wires more securely in place. The Stycast also provides a good thermal link without electrical conductivity. By using the monolithic design, two

drawbacks seen in the coil-SQUID combination are eliminated, impedance mismatch and spatial averaging. An impedance mismatch between the pickup coil and the transformer circuit that delivers the measured flux to the SQUID limits the field sensitivity of the SQUID. The cylindrical coil stack results in a spatial averaging on the coil axis that degrades the spatial resolution since not all coils are as close to the sample as others. The monolithic SQUID sensor has both the SQUID and feedback line on one plane, correcting for these effects.[10,11,11,12,26,49,54]

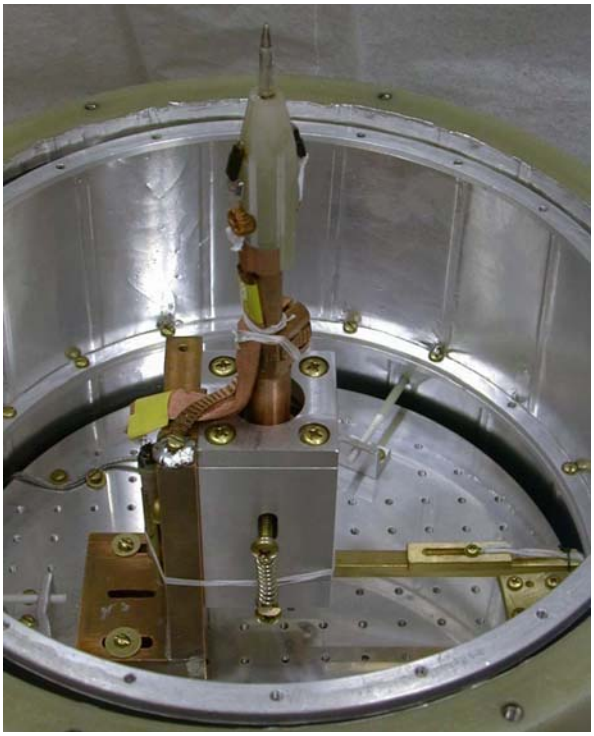

Figure 13 The monolithic chip is mounted on a sapphire rod that clamps into the lever mechanism inside the SQUID Dewar.

Magnetic shield and stage

The SQUID microscope is placed in a magnetically shielded room[1,55-58] on a support structure above a nonmagnetic scanning and leveling stage. The magnetically

shielded room (Vacuumschmelze) consists of two layers of μ-metal to reduce magnetic interference, including DC and higher frequency noise sources.

The support structure, a 2-foot high, wooden horse, seen in Figure 14, sits above a leveling stage. The leveling stage first aligns the room temperature sample parallel to the SQUID window, using a tripod configuration of stepping motors. It then uses two magnetically-shielded, precision piezoelectric inchworm motors that scan the sample in an x-y raster pattern underneath the SQUID to collect the magnetic data. The stage has a total scanning range of about 50 mm in both x and y directions with a resolution of 0.5 μm.[1,7,12,44,59]

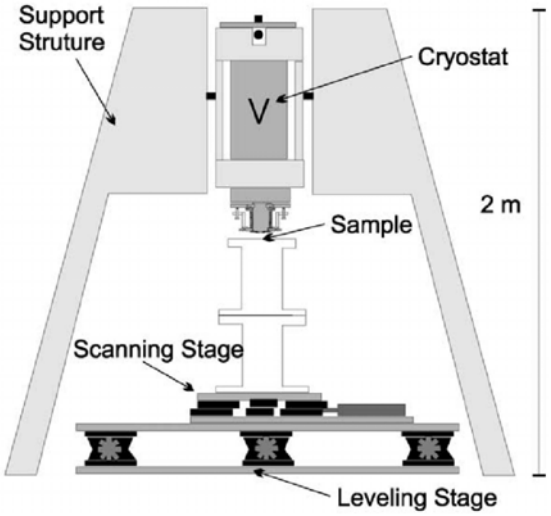

Figure 14 SQUID microscope support structure with the scanning stage for the sample.[1]

Optimization of monolithic SQUIDs

There are two different types of thin-film niobium monolithic SQUID sensors fabricated by HYPRES that have been tested at Vanderbilt: the bare SQUID and the cartwheel SQUID design. This section will discuss the optimization process of the bare and multiloop SQUIDs.

The monolithic SQUIDs are fabricated at HYPRES using a sputtering technique for niobium thin films. Once there is a thin coat of niobium, the thin films are formed into the designs of choice using photolithography or electron-beam lithography. This is done using a tri-layer process of $Nb/NbO_x/Pb$ or $Nb/Al_2O_3/Nb$. The current process produces Josephson junctions with a minimum diameter of 3.5 μm, which results in a self-capacitance of 0.4 pF/ junction. The design for the bare and multiloop SQUIDs are shown in Figure 15 and Figure 16 respectively. The washer (the pickup loop) and SQUID combination attach to two of the gold contact pads and the feedback loop attaches to the other two gold pads.[10,21,24,40,46,60,61]

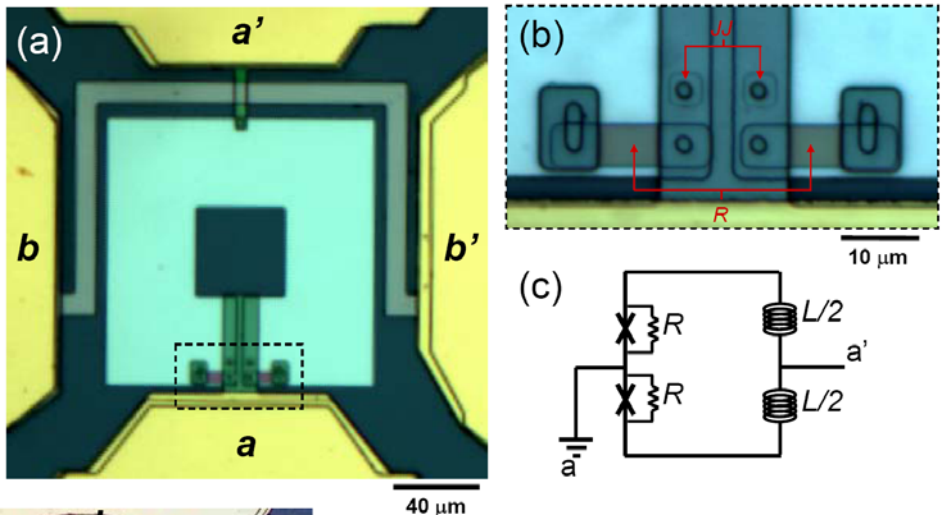

Figure 15 The monolithic bare SQUID design. a) The SQUID washer connects to gold pads a and a' and the feedback loop connects to pads b and b'. b) The Josephson junctions and shunt resistors. c) A schematic of the SQUID design.[12]

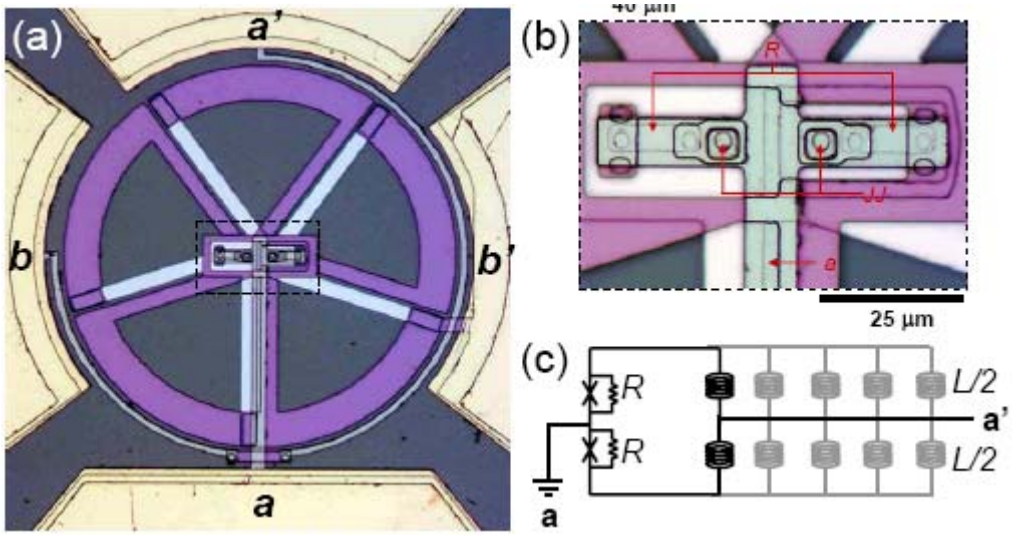

Figure 16 The monolithic multiloop SQUID design. a) The SQUID washer connects to gold pads a and b' and the feedback loop connects to pads a' and b. b) The Josephson junctions and shunt resistors. c) A schematic of the SQUID design.[12]

Because the key to a good working SQUID is its noise performance and field sensitivity, the optimization process should provide the highest signal-to-noise ratio possible while minimizing the amount of detectable field per unit of bandwidth. The flux noise corresponding to the SQUID loop can be calculated using the equation

$$S_\phi(f) = \frac{S_V(f)}{\left(\frac{\partial V}{\partial \Phi}\right)^2} \tag{5}$$

where the spectral density from the noise across the SQUID is

$$S_v(f) = \frac{16 k_B T L^2}{R_n} \tag{6}$$

where f is the frequency, V is the voltage across the SQUID, k_B is the Boltzmann's constant, T is the temperature of operation, L is the inductance, and R_n is the shunt resistance.

The voltage-to-flux conversion part of the flux noise is related to the shunt resistance R_n and SQUID inductance L. This is shown as

$$\frac{\partial V}{\partial \phi} \approx \frac{R_n}{L} \tag{7}$$

Therefore, the flux sensitivity becomes

$$S_\phi(f) \approx \frac{16 k_B T L^2}{R_n} \tag{8}$$

The noise optimization relies much on the inductance, which is proportional to the size of the bare SQUID sensor given by

$$L = 1.25 \mu_o h \tag{9}$$

where h is the diameter of the SQUID sensor's hole and μ_0 is the permeability of free space.[10] For the multiloop SQUID sensor the inductance

$$L = \frac{L_p}{N^2} + \frac{L_s}{N} + L_j \tag{10}$$

where L_p is the inductance without spokes (which is proportional to area of the sensor), L_s is the inductance of one spoke, L_j is the small parasitic inductance of the Josephson junction connection lines and N the number of spokes. This means that the SQUID sensitivity is also proportional to the effective area of the SQUID, which is given by

$$A_{eff} = (h + w)^2 \tag{11}$$

for the bare SQUID sensor where w is the width of the washer and

$$A_{eff}^* = \frac{A_p}{N} - A_s \tag{12}$$

for the multiloop SQUID sensor where A_p is the area of the circular coil without spokes, A_s is the area of one spoke, and N is the number of spokes. Therefore, the sensor size must be adjusted so that the minimum desired flux noise is obtained. It is clear that the inductance should be reduced, while the resistance should be increased, in order to improve the noise performance due to the inductance's dependence on sensor area.[10-12,40,54,62] However, a SQUID sensor of larger area gives us a higher sensitivity, which also increases the noise. Again, this is the trade-off between sensitivity and spatial resolution. A SQUID sensor must be optimized for its desired performance in a given experiment, such as using larger area multiloop SQUID sensors for high sensitivity experiments, as in weak biological samples,[12,19,27,30,47-49] or small area bare SQUID sensors for small spatial resolution experiments, as in geological samples.[12,44-46]

Two more considerations that must be taken into account when optimizing the SQUID are parameters β_C and β_L ,

$$\beta_C = \frac{2\pi I_C R_n^2 C}{\phi_o} \leq 0.7 \tag{13}$$

$$\beta_L = \frac{2LI_C}{\phi_o} \cong 1 \tag{14}$$

where *Ic* is the critical current, *C* is the Josephson junction capacitance, and Φ_o is one flux quantum (2 x 10^{-15} Wb). The parameter β_C must be less than 0.7 to eliminate hysteresis and provide a single valued voltage across the SQUID from an applied external field. This puts a limit on what values can be used for the resistance without going outside the limit values of β_C. The parameter β_L is called the reduced inductance that is a measure of modulation depth of the critical current as a function of applied flux. For optimum performance of the SQUID, β_L must be close to the value 1.[10,63-66]

The steps for optimizing SQUID sensors are as follows. Because the inductance is determined by the size of our SQUID sensors, the larger SQUID dimensions will have a higher inductance. We have found that the maximum diameter of a bare SQUID should be less than 250 μm due to increase in noise at larger diameters. Once the size of the sensor is decided, the shunt resistance is adjusted to lower the flux noise, yet the parameter β_C is kept less than 0.7. By using these parameters, we have developed some designs that are useful for our SQUID measurements. Four designs with their parameters and properties are listed in Table 1. The sizes of the SQUIDs are labeled by the length of the hole h and washer width w.

Table 1 Bare SQUID design parameters and properties.

Name	h (μm)	w (μm)	A_{eff} (mm^2)	L (pH)	I_c (μA)	R_n (Ω)	ΔV (μV)	$S_\Phi^{1/2}$ ($\mu\Phi_0/Hz^{1/2}$)	$S_B^{1/2}$ ($pT/Hz^{1/2}$)
BR01	20	20	$3.62*10^{-3}$	29.1	6.34	9.7	52	1.19	0.7
BR04	40	10	$7.37*10^{-3}$	81.9	8.31	10.6	40	2.85	0.8
BR03	40	20	$9.25*10^{-3}$	69.7	4.35	10.4	29	6.77	1.4
BR10	30	60	$1.13*10^{-3}$	32.8	8.22	12	49	2.68	0.5

Pickup coil coupled SQUIDs

The hand-wound pickup coil coupled SQUID uses a pickup coil that detects the samples field, and then couples the signal into the SQUID. This type of SQUID design has a field sensitivity, which uses a pickup coil (^{p}), of

$$B^{(p)} = \frac{\sqrt{S_\phi^p}}{n\pi r_p^2} \tag{15}$$

where the flux noise of the pickup coil is

$$S_{\phi}^{(p)} = \frac{2(L_i + L_p)^2 \varepsilon}{L_i \alpha^2} \tag{16}$$

where n is the number of loops, r_p is the radius of the pickup coil, L_i is the input coil inductance, L_p is the pickup coil inductance, ε is the SQUID energy sensitivity, and α is the coupling coefficient between the input coil and the SQUID.[1,7,26,28,29,33,49,54]

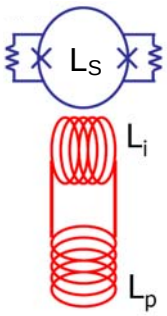

Figure 17 A schematic of the hand-wound pickup coil coupled SQUID with the SQUID inductance L_S, the input coil inductance L_i, and pickup coil inductance L_P.

The 500 μm diameter pickup coil coupled to the SQUID has specifications that are acceptable for making cardiac magnetic field measurements. It has a measured noise of about 3 $\mu\Phi_0/Hz^{1/2}$, a field sensitivity of approximately 300 $fT/Hz^{1/2}$, and a spatial resolution around 500 μm (which is roughly the size of the pickup coil).

Characterization of SQUIDs

In order to determine the best optimization for our SQUID sensor, the SQUIDs must be characterized by their intrinsic properties and noise and field sensitivity measurements. In order to completely characterize the SQUID, we must obtain its current versus voltage curve, voltage per flux quantum plot, and a frequency analysis of the noise and field sensitivity.

The current versus voltage curve is obtained by applying a range of currents in the form of a triangle wave. The voltage is obtained from the applied current. The current is swept from negative to positive and then positive to negative current. This tests for hysteresis and should give a single value voltage for each current. Two intrinsic parameters can be found from this current versus voltage plot, the critical current and shunt resistance. The critical current is the maximum or minimum current that results in zero voltage, where a voltage drop occurs. The shunt resistance is simply twice the slope of the nonzero current versus voltage.[19,26,28,29,33] This plot is shown in Figure 18.

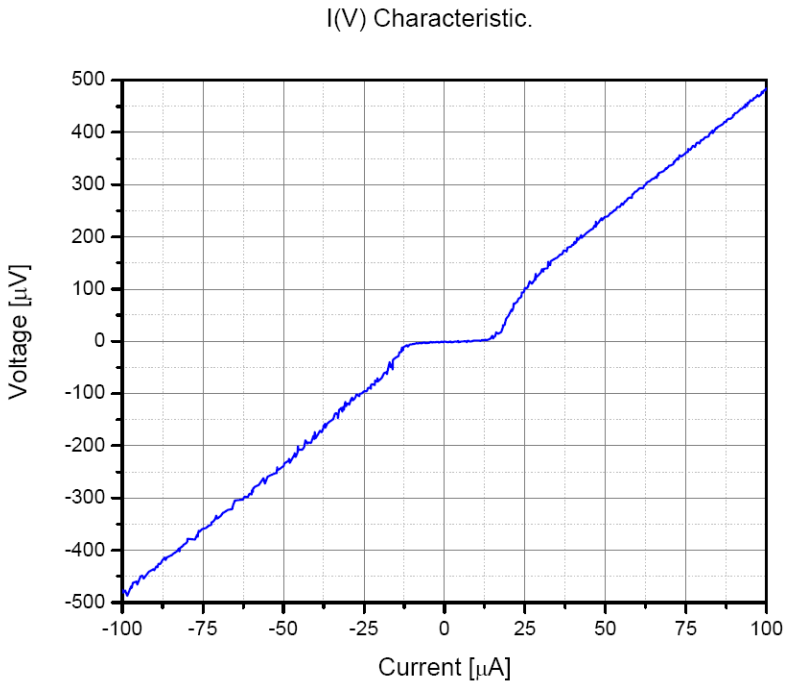

Figure 18 *I(V)* Characteristic for a h = 20 μm, w = 20 μm bare SQUID. I_c is 6.34 μA; and R_n is 9.73 Ω.

The voltage per flux quantum is found by applying a triangular wave through the feedback loop, while sending a constant bias current through the SQUID. The bias current should be adjusted until the largest change in voltage occurs, the maximum modulation voltage ΔV. This plot can be seen in Figure 19. The mutual inductance

between the feedback line and SQUID can also be calculated from this plot. It is calculated using the equation $M = \Phi_o/I$, where the current per flux quantum is the measurement of the amount of current in one period on the graph. [19,26,28,29,33]

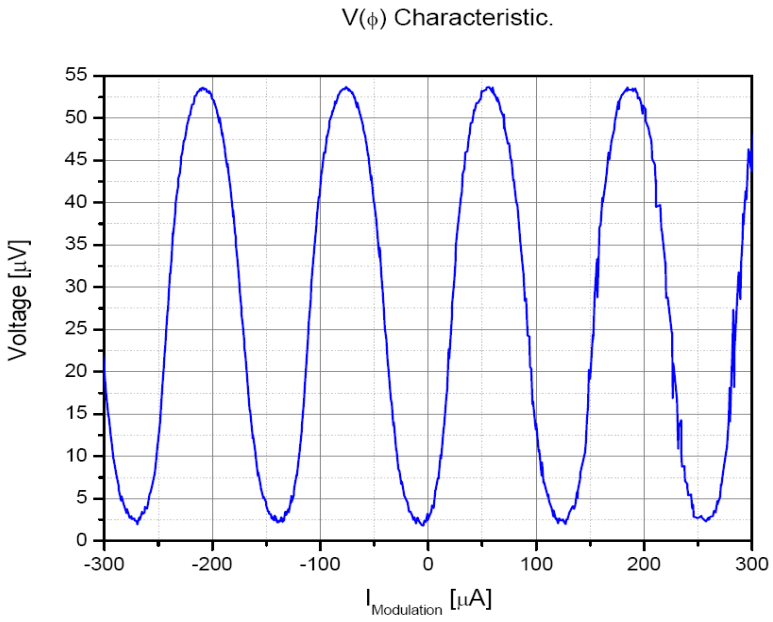

Figure 19 *V(Φ)* Characteristic for a $h = 20$ μm, $w = 20$ μm bare SQUID. Δv is 49.1 μV; I/Φ_o is 67.8 μA; and M is 30.5 pH.

In order to measure the noise performance, we must set the SQUID in a flux-locked-loop as previously described. The SQUID must be magnetically shielded to operate the sensor in the high sensitivity regime. The SQUID output is then measured with a spectrum analyzer to obtain the noise spectrum. The noise of the SQUID is composed of mainly Johnson noise. At low frequencies there is 1/f dependence that can be related to trapped flux in the SQUID itself or fluctuations in the critical current of the Josephson junctions. At higher frequencies, white noise is more apparent until the roll-off frequency of the flux-locked-loop electronics.[7,26,40,67-71] An example of the measured noise spectrum is shown in Figure 20.

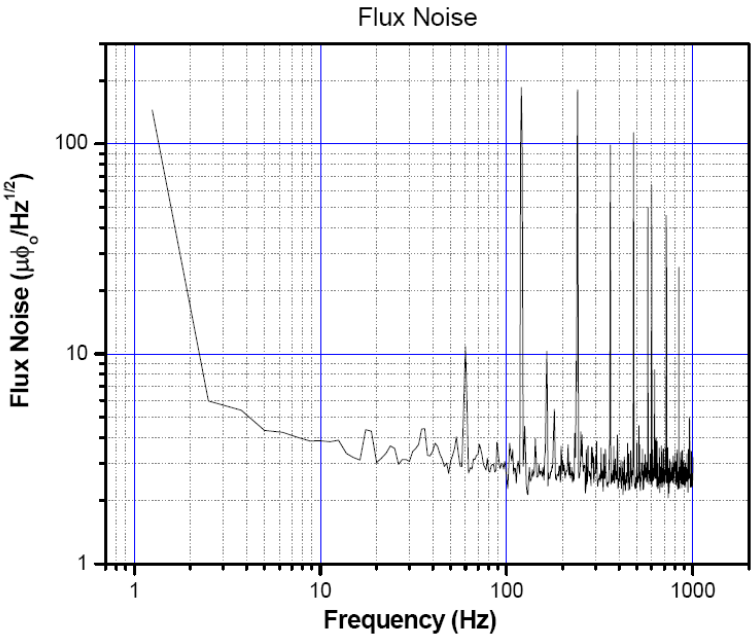

Figure 20 Flux noise for a h = 20 μm, w = 20 μm bare SQUID. At the frequency of 100 Hz the flux noise is 3.0 μ□$_0$/Hz$^{1/2}$.

The field sensitivity is known as the minimum detected field per unit bandwidth. It is measured using a Helmholtz coil. The SQUID sensor is placed in the center of the Helmholtz coil. A known magnetic field is applied to the SQUID sensor, which then returns an output voltage in response to the applied field. A value of voltage per Tesla is obtained and is used to calculate the field sensitivity from the noise spectrum, as shown in Figure 21.[23,24,28,29,31,33,40]

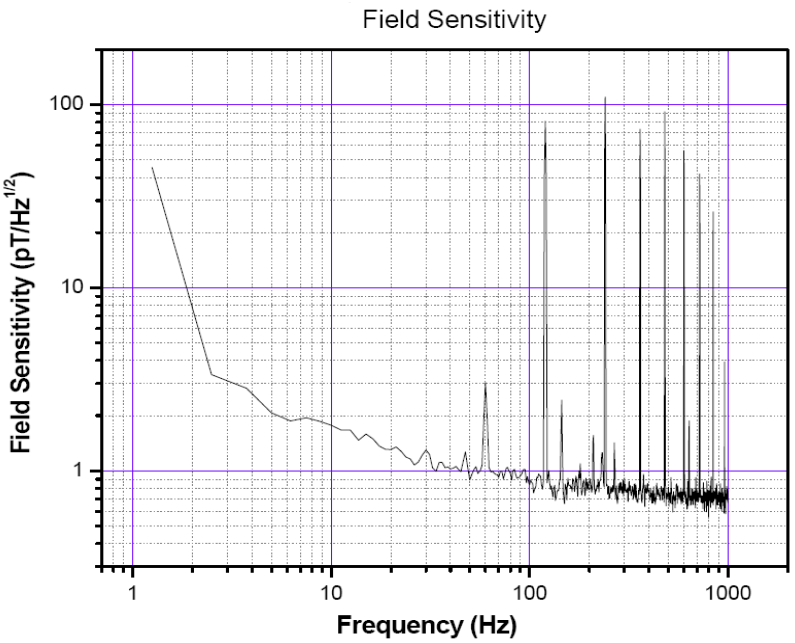

Figure 21 Field sensitivity for a h = 20 μm, w = 20 μm bare SQUID. At 100 Hz the field sensitivity is 0.85 pT/Hz$^{1/2}$.

CHAPTER III

MEASUREMENTS OF CARDIAC ACTION POTENTIAL PROPAGATION IN THE SPIRAL FIBER ORIENTATION OF THE APEX USING OPTICAL MAPPING AND SUPERCONDUCTING QUANTUM INTERFERENCE DEVICE MICROSCOPY

Abstract

The transmembrane potential and magnetic fields from electrical activity of the apex of the isolated rabbit heart have been studied experimentally using epifluorescent imaging and Superconducting Quantum Interference Device (SQUID) microscopy and theoretically using monodomain and bidomain modeling techniques. The cardiac apex has a complex spiral fiber architecture that plays an important role in the development and propagation of action currents during stimulation at the apex. This spiral fiber orientation contains both radial electric currents that contribute to the electrocardiogram (ECG) and "electrically silent" circular currents that cannot be detected by the ECG but are detectable by their magnetic field, B_z. In our experiments, the transmembrane potential, V_m, was first measured optically, and then B_z was measured with a SQUID microscope. While the circular V_m wave fronts were detected, the B_z maps were not as expected. Based upon a simple model of the spiral structure of the apex, V_m was expected to exhibit circular wave front patterns and B_z to reflect the circular component of the action currents. However, we observed a pattern consistent with a tilted axis for the apex spiral. We were able to simulate similar patterns in both a monodomain model of a tilted stack of rings of dipole current, and in a bidomain model of a tilted stack of spiraled cardiac tissue that was stimulated at the apex. The fact that the spatial pattern of the

magnetic data was more complex than the simple circles observed for V_m suggests that the magnetic data contain information that cannot be found electrically.

Background

The heart has a very complex structure that regulates action potential propagation. The cardiac cells are brick-like and cylindrical, with a diameter of about 15 μm and a length of about 100 μm. They are connected by intercalated disks that contain both desmosome and gap junctions. The desmosome junctions mechanically attach the cells together, while the gap junctions, which have a low electrical resistance, allow for the cell-to-cell transfer of ions that cause the action current and action potential propagation[72] These connections between different cells cause the cardiac tissue to behave as a functional syncytium.[13,19] Each cardiac cell is arranged in a staggered aperiodic arrangement rather than in a regular repeating pattern.[72] It has been found that cardiac myocytes form distinct layers separated by voids[6,73] and having distinct fiber orientations, which twist and turn throughout the heart structure.[6]

The flow of action current patterns throughout the heart determines how the heart is activated and subsequently contracts. For point electrical stimulation of the heart that doesn't involve the cardiac conduction system, the complex fiber orientation of cardiac tissue determines the activation of the tissue and the spread of the action currents and potentials in the heart. Many experiments have been conducted on the heart, but much remains to be understood regarding the effects of cardiac tissue structure on the propagation of action currents.[2,6,74]

Complementary measurements of the ECG and magnetocardiogram (MCG) could be an important gauge for determining heart condition.[17] Currently, the ECG is used clinically to examine heart cardiac abnormalities and disease; however, with the help of the MCG, additional diagnostic information could be found in the electrically silent but magnetically detectable components of cardiac electrical activity.[16,75]

Cardiac electrophysiology has been studied in detail using arrays of extracellular or intracellular microelectrodes.[76] However, microelectrodes are limited to point measurements. It is difficult and cumbersome to obtain multisite recordings simultaneously due to the contractile nature of the heart and the need for multichannel data acquisition.[77-79] Also, microelectrode techniques tend to be invasive.[80] Over the past sixteen years, noninvasive epifluorescence measurements using voltage-sensitive dyes have been established to image transmembrane action potential distributions. These optical mapping techniques produce spatiotemporal potential maps with millimeter spatial resolution and frame rates as high at one kilohertz. However, the intra- and interstitial potentials depend on the variations of the transmembrane potential throughout the tissue.[81-85]

Though one imaging modality, either epifluorescence or magnetic microscopy, is sufficient for one-dimensional studies of V_m and B_z for a single axon, it may not be sufficient to make accurate predictions in three-dimensional cardiac studies, due to anisotropic conductivities and complex fiber structure.[86,87] Using a combination of epifluorescence optical imaging techniques and Superconducting Quantum Interference Device (SQUID) microscopy, along with an established protocol for imaging action current distributions in isolated Langendorff-perfused whole hearts, both the V_m and B_z

can be measured though not simultaneously.[1,7,9,88,89] By using these multimodal experimental techniques with monodomain and bidomain modeling, it is possible to study cell-to-cell communication in the heart on the tissue level.

It has been determined that the ventricles of the heart have a relatively parallel fiber orientation with a slow rotation into the deeper layers. Because of the wrapped, multilayered arrangement of cardiac fibers, the apex has a much more complex fiber orientation than the ventricular free wall, in that the fibers spiral and rotate around the apex of the heart, as shown in Figure 22.[13-15,90]

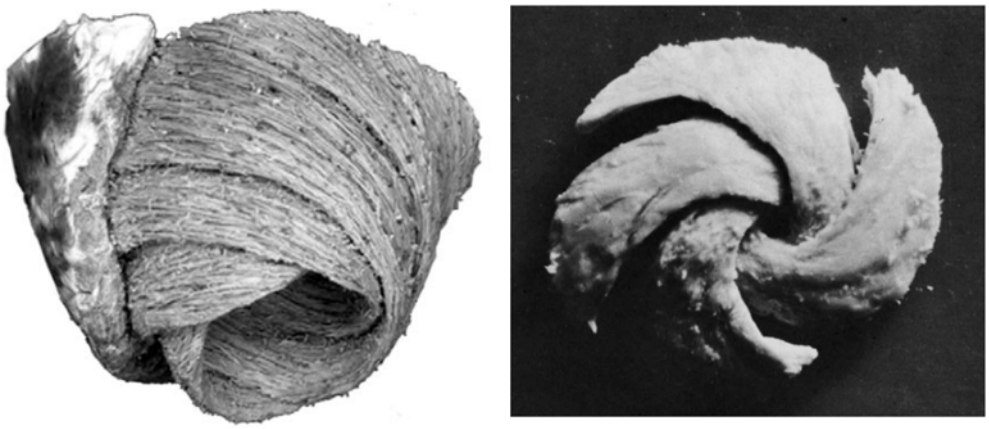

Figure 22 The wrapped multi-layer spiral structure of the apex.[14,15]

A comparison of the fiber structures for the left ventricle wall and apex is illustrated in the cartoon in Figure 23. The left ventricle free wall has a straight fiber orientation, while the left ventricle apex has a spiral structure.[6,13] Figure 23a-b also shows the wave front propagation (shown in sections a and b) that would occur from such fiber orientations if they were stimulated at the central point of the structure. The left ventricle's wave front propagation has an elliptical shape which shows wave front propagation faster along the fiber direction than transverse to the fiber orientation.[89] The

apex has a radial wave front propagation due to spiral symmetry.[75] The magnetic field patterns are also shown in Figure 23c-d for both the left ventricle free wall and apex.

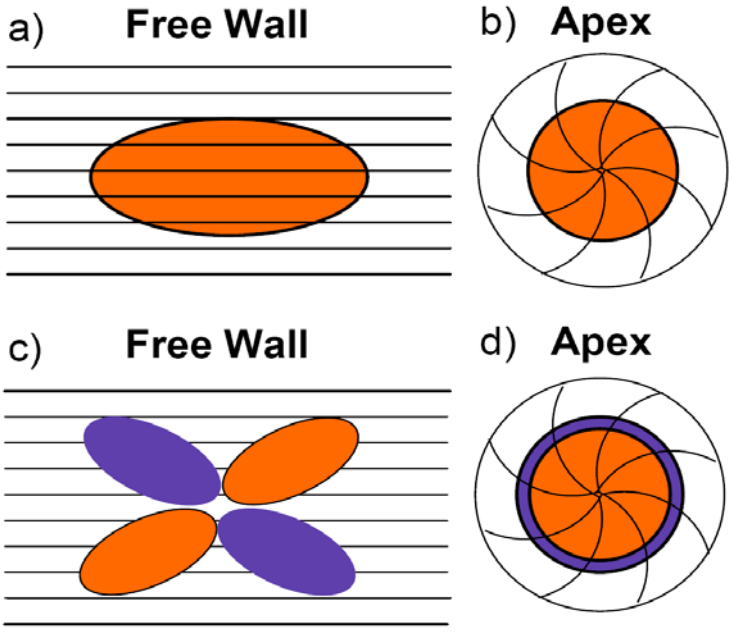

Figure 23 Representations of cardiac fiber structures of the left ventricle free wall and apex. The black lines represent fiber direction. a-b. The red oval and circle represent wave front propagation. c-d. The red and blue ovals and circles represent the magnetic field patterns with respect to the action current propagation, where red and blue are opposite magnetic field polarities.

The left ventricle has been studied magnetically in greater detail than any other part of the heart due to its less complicated, locally parallel fiber geometry.[11,12,17,91-93] Measurements by Holzer *et al.* using epifluorescent and SQUID imaging on the left ventricle free wall with central cathodal stimulation revealed the elliptical wave front pattern from the membrane potential (Figure 24), which has the major axis along the fiber direction, as expected due to longitudinal and transverse fiber tissue conductivities.[94] The elliptical pattern was also reflected in the action current magnetic images in the SQUID data, which started out as a magnetic quatrefoil stimulus pattern.[1,89,95-97] Again, the elliptical pattern has the major axis along the fiber direction[89] (indicated by an arrow in the 11 ms data frames of Figure 24).

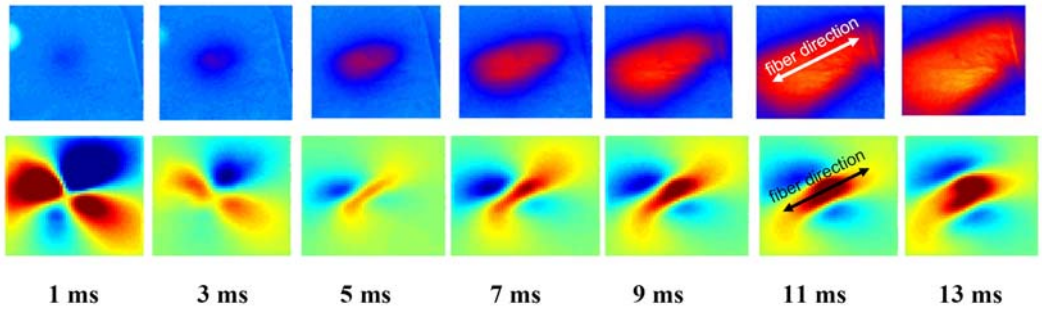

Figure 24 Left ventricle (parallel surface fibers) experimental data. Top: Transmembrane potential elliptical pattern. Bottom: Magnetic field image with quatrefoil magnetic stimulation pattern and elliptical propagation pattern. Fiber direction is estimated for the 11 ms data.

In contrast to the extensive studies of the left ventricle, little work has been done to compare the electric and magnetic activation patterns of the apex, due to its complex fiber structure. As a result of the spiral structure, circular propagation of the transmembrane potential is expected to produce electrically silent currents. Diagnostic information can be extracted from these electrically silent fields by imaging their magnetic fields. Roth and Wikswo have previously calculated these silent currents from the apex that arise from the spiral curvature.[16,75,98]

Through a combination of epifluorescent and SQUID imaging, the electrically silent action currents can be studied experimentally. The membrane potential is found using epifluorescent imaging to measure the action potential propagation (Figure 25) of the apex at many simultaneous points. This allows the radial components of the activation wave front to be seen. Not only is the wave front obtained, but the scanning SQUID microscope can sequentially measure the MCG (Figure 25) at multiple points above the apex. These MCG recordings include the electrically silent circular currents that cannot be detected by the ECG.[16,75,98]

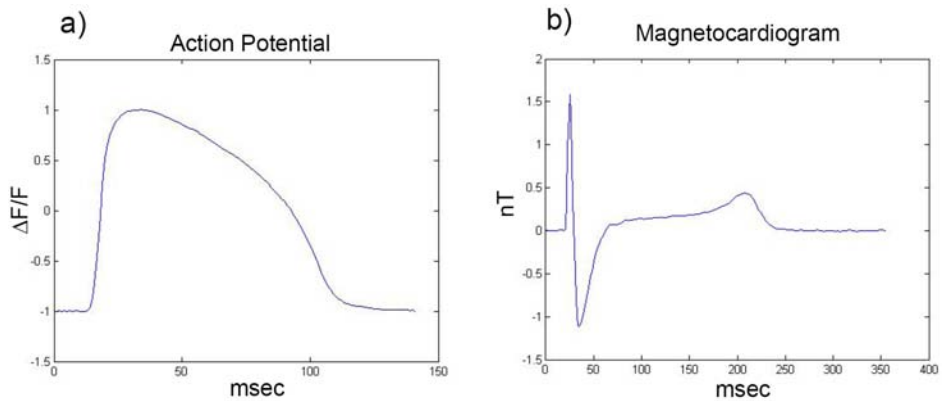

Figure 25 Experimental data at one point on surface of the apex. a) The apex transmembrane potential from epifluorescent imaging. b) The apex magnetocardiogram from SQUID microscopy.

Additionally, the data are interpreted using both monodomain and bidomain modeling. The data obtained from these measurements show that the pattern of wave front propagation of V_m is not the same as the pattern for action current propagation of B_z.

Methods and materials

Cardiac Preparation

All experiments were conducted in accordance with National Institutes of Health regulations for the ethical use of animals in research and approved in advance by the Vanderbilt Institutional Animal Care and Use Committee.

The hearts used in this experiment were extracted from New Zealand white rabbits that weighed on average 3–4 kg. The rabbit was first preanesthetized through an injection of intramuscular ketamine (50 mg/kg) into one of the hind leg muscles. Once the rabbit was sedated, it was placed in a restraint device and then injected with 2000 units of heparin and anesthetized with sodium pentobarbital (50 mg/kg) by way of the main ear vein. All injections were conducted without bubbles in the solution to eliminate

irregular blood flow. Once the rabbit was anesthetized, the heart was rapidly excised by a midsternal incision.[89] The heart was immediately mounted on a Langendorff perfusion system for retrograde aortic perfusion with oxygenated Tyrode's solution containing 130 mM NaCl, 4 mM KCl, 1.5 mM NaH_2PO_4, 10 mM glucose, 23 mM $NaHCO_3$, 1 mM $MgCl_2$, and 2 mM $CaCl_2$, which is adjusted to a pH of 7.40 ± 0.05 with 1 M NaOH. The perfusate solution was constantly saturated with 95% O_2/ 5% CO_2 gas mixture and was kept at a temperature of 37°C for the duration of the experiment.[99,100]

To prepare for the apex experiments, the left atrium was first cut to expose the mitral valve. The isolated Langendorff-perfused heart was then mounted upside down on a Teflon post in an open acrylic chamber that contains the temperature-controlled perfusate bath. The Teflon post, which has a hole through its center for electrode placement, was inserted first into the left atrium and then through the mitral valve into the left ventricle in order to hold the heart in place. The acrylic chamber was supported by a pedestal that allowed easy transfer of the heart between the optical and the magnetic measuring setups. An electromechanical uncoupling agent, 2,3- butanedione monoxime (also known as BDM or diacetyl monoxime; Sigma, St Louis, MO), was added to the perfusate solution at a concentration of 15 mM to block muscle contraction,[89] which helped suppress most motion artifacts that could occur in the experimental data. A bipolar electrode was threaded through the hole of the Teflon post until it was about 50 μm from the surface of the apex of the heart. A 10 μm thick Mylar film was attached to the acrylic dish to protect the heart during scans. The electrode was constructed using a 100 μm diameter silver wire inside a 1 mm diameter brass tube. The setup is shown in Figure 26. The electrical stimulation was provided by a computer-controlled current source (Bloom

Associates, Narberth, PA). The heart was paced at a 350 ms cycle length with 4 ms electrical stimuli. The amplitude of the stimuli was approximately 0.6 mA, just above the diastolic stimulation threshold, but not strong enough to induce visible virtual electrode patterns.

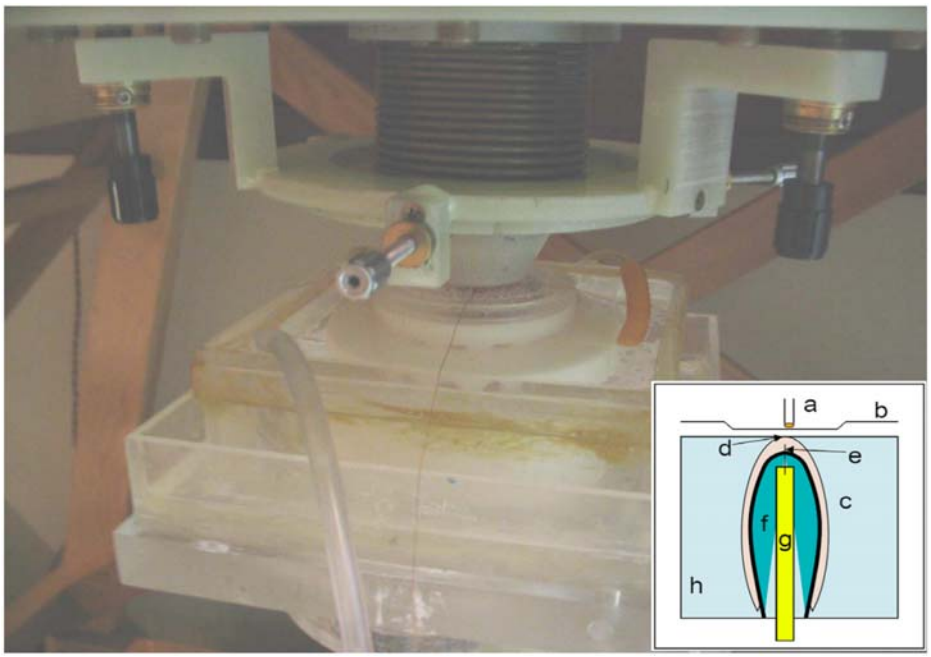

Figure 26 Experimental setup for measuring the apex under the SQUID microscope. Inset: Apex stimulation setup: a. SQUID sensor pickup coil, b.SQUID microscope Dewar tail, c. heart, d. apex, e. cathodal electrode, f. Teflon post, g. anodal electrode, h. perfusate bath. The cathodal stimulation occurred approximately 50 μm below the surface of the apex.

Spatial registration becomes important in the comparison of images from both fluorescent and magnetic experimental measurements. The spatial arrangement was marked by two thin wires that were placed perpendicular to each other across a corner of the imaging area, as shown in Figure 27. The wires were then imaged optically along with a ruler marked in millimeters. Magnetic registration was achieved by applying a small current through each individual wire, which is imaged magnetically using the SQUID microscope. Each magnetic recording was a measurement of the magnetic field

as a function of position. When both individual wire images were combined, a zero-crossing of the magnetic field provided the location of the wire relative to the magnetic image. This zero-crossing was also located in the optical images. With this technique, the two sets of images were aligned with an accuracy of approximately 0.5 mm.[89]

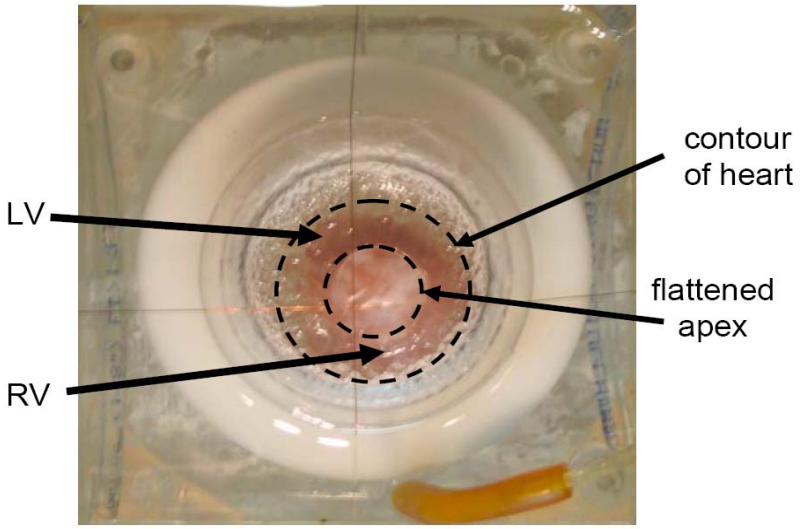

Figure 27 Experimental setup of heart in the pedestal bath with the apex facing up. Left ventricle (LV) and right ventricle (RV). The crossed wires are for alignment. The dotted circles show the flattened apex relative to the contour of the heart.

Optical imaging and data analysis

The first experimental measurements were taken using the optical imaging system, previously described by Sidorov *et al.*, which recorded the transmembrane potential. The hearts were stained with 200 μL of the mixed solution containing 5 mg voltage-sensitive styryl dye di-4-ANEPPS (Molecular Probes, Eugene, OR) and 10 ml dimethyl sulfoxide. A two Watt diode-pumped, solid-state laser (Verdi, Coherent, Santa Clara, CA) with a wavelength of 532 nm was delivered to the apex through a set of fiber optic bundles. The laser light was used to excite the voltage-sensitive dye, causing fluorescence. The fluorescence was imaged using a high-speed CCD camera (Model CA

D1-0128T, Dalsa Inc, Waterloo, ON, Canada) filtered by a 607 nm cutoff filter (#25 Red, Tiffen, Hauppauge, NY). The image data were acquired at 2 ms intervals with a 12-bit resolution over a 128 × 128 grid of pixels corresponding to a 12 mm × 12 mm area. The digital images were transferred to a Bitflow R3-DIF image acquisition board (Boston, MA) in a Dell 650 Pentium IV/2 GHz Precision workstation.[89,99]

The voltage-sensitive dye allowed us to measure the ratio of the change in fluorescence intensity from the excited tissue, ΔF, to the fluorescence intensity from the diastolic (resting) tissue F_D, also known as $-\Delta F/F_D$. The negative sign corrects for the decrease in the intensity of fluorescence with a more positive potential.[89] The optical data presented in this chapter has been additionally preprocessed by employing a 5 × 5 Gaussian spatial filter and a five-point mean temporal filter.[99]

Magnetic imaging and data analysis

After the optical measurements were taken, the pedestal containing the heart and bath were moved from the optical recording setup and quickly placed on the scanning stage under the SQUID microscope, shown in Figure 26, to measure the B_z field associated with the action currents from the action potential propagation. The SQUID microscope used a pickup coil to directly couple the B_z field to the flux transformer of the SQUID sensor. The pickup loop consisted of 20 turns of 25 μm diameter niobium wire wound in two layers around a 500 μm sapphire bobbin on tip of a 1 mm diameter, 4 cm long sapphire rod. The sapphire and bobbin were mounted in the tail of the SQUID microscope, and when under vacuum was maintained at ~5.8 K by a thermally coupled liquid helium reservoir. The pickup coil was positioned about 300 μm from a 25 μm thick

sapphire window that separates the vacuum from the outside atmosphere. This SQUID microscope configuration provided a magnetic field sensitivity of 608 $fT/Hz^{1/2}$. The SQUID microscope used is discussed further in Baudenbacher *et al.*[1,7]

The SQUID microscope window touched the heart slightly (without damaging it) during the scans, resulting in a sensor-to-window to sample distance of ~325 μm. The SQUID was operated in a flux-locked loop at a bandwidth of 1 kHz (DC-5000 controller, Quantum Design, San Diego, CA). The output was collected using a PCI-MIO card (National Instruments) with 16-bit resolution at a sampling rate of 5 kHz. The data acquisition was triggered by the stimulation pulse, which was controlled using a LabVIEW computer program. The x-y raster scan was also controlled by the LabVIEW program. Magnetic action potential fields were recorded at 0.5 mm steps in the x-y raster scan. The magnetic action potential fields were then combined using the stimulus pulse for synchronization in order to produce a time series of two-dimensional magnetic field maps. The time interval between successive field maps was 1 ms, given by the bandwidth of the flux-locked loop electronics. Because the data acquisition was triggered at the rising edge of the 4 ms stimulation pulse, the termination of stimulus was determined with an accuracy of 1 ms. This allowed synchronization of the magnetic and optical data to an accuracy of 2 ms. The magnetic data was then spatially filtered with a rotationally symmetric Gaussian low-pass filter of 2.5 mm size with a standard deviation of 0.5 mm. The 5 kHz bandwidth of the measured magnetic data was reduced to 1 kHz bandwidth by computing the mean of five sequential data points.[89]

Monodomain Model

The apical magnetic field pattern was estimated by a numerical monodomain model comprised of a stack of spiral discrete current dipoles that represented the cardiac apex structure. The law of Biot-Savart was used to calculate the B_z field for a stack of ten rings containing 100 discrete angled, current dipoles, as shown in Figure 28. The ring had a diameter of 600 μm, and the stack height was 1 mm . The grid step size was 3 μm, with a discretization of 200 points. Figure 28 shows a single ring of 100 current dipoles with an angled orientation of 33 degrees (shown more clearly in the enlarged inset).

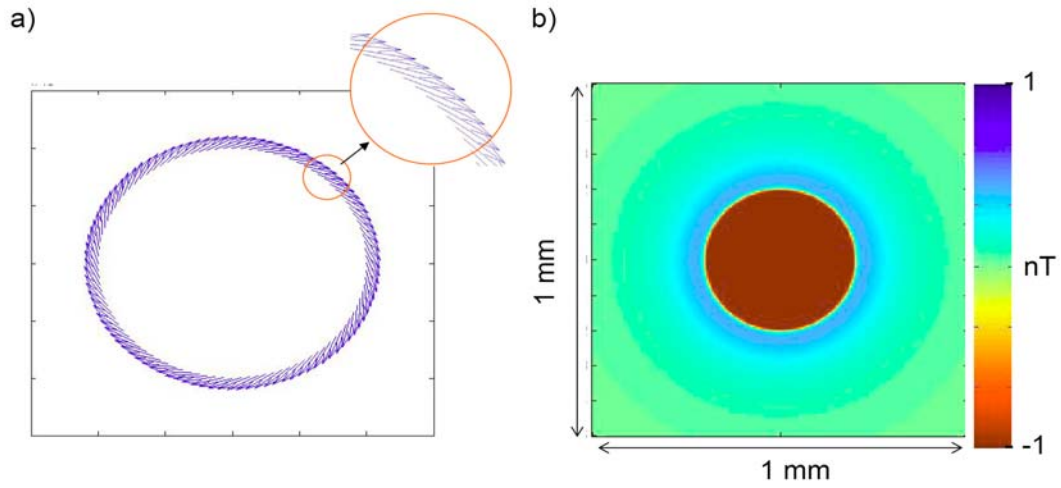

Figure 28 a) Monodomain model of a ring of 100 current dipoles angled at 33º at a radius of 600 μm. b) Calculated magnetic field from a stack of 10 concentric rings spanning a depth of 1 mm.

Bidomain Model

A more precise nonlinear, time-dependent bidomain model with spiral symmetry provided a finite-difference solution to the doubly-anisotropic bidomain equations.[101] The equation for the transmembrane potential was solved using a forward Euler explicit method, with the membrane kinetics represented by the Beeler-Reuter model.[102] The equation for the extracellular potential was solved using successive over-relaxation.

Several of the parameters used in the calculation are given in Table 2. The intracellular and extracellular conductivity tensors depended on location via the angle θ between the x-axis and the fiber direction.[94] The fibers were oriented as a logarithmic spiral,[75] with an angle of 45° to the radial direction. The center of the spiral represents the apex of the heart. In some cases, the location of the center of the spiral depended on depth (a "skewed stack"). The stimulus was applied through a small unipolar cathode (0.25 mm diameter) on the epicardial surface, with the return electrode being a 1.5 mm diameter anode on the endocardial surface. Except under the electrodes, all surfaces were sealed. The stimulus strength was 0.6 mA, and the stimulus pulse had a duration of 43 ms. The tissue slab was 10 mm × 10 mm in area (x, y), and 2 mm thick (z). The space step was 0.1 mm in the x and y directions, and 0.05 mm in the z direction. The time step was 10 microseconds. The magnetic field was calculated by numerically integrating the Biot-Savart law over the tissue volume. Only the z-component of the magnetic field was calculated, over a plane 0.5 mm above the epicardial surface.

Table 2 Bidomain Parameters

Intracellular longitudinal conductivity	0.1863 S/m
Intracellular transverse conductivity	0.0179 S/m
Extracellular longitudinal conductivity	0.1863 S/m
Extracellular transverse conductivity	0.0894 S/m
Surface-to-volume ratio	0.3×10^6 m^{-1}
Membrane capacitance	0.01 F/m^2

Results

Experimental measurements were performed to detect, using epifluorescence, the expanding, circular V_m wave front as it propagated outward from the electrode, and, using

SQUID imaging, the corresponding B_z pattern. A 12 mm × 12 mm section of the cardiac apex was examined, and the results are shown in Figure 29. The first row shows V_m images that demonstrated the wave front propagation that results from electrical stimulation at the apex, while the second row shows the B_z images from the magnetic field associated with action currents. The 2 ms time steps start 1 ms after the end (release) of the cathodal stimulus. The measured amplitude of the B_z field is in nT.

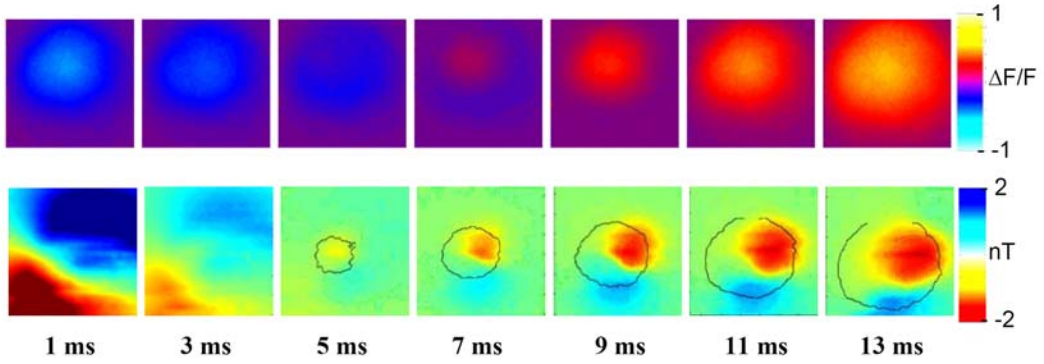

Figure 29 Experimental data recorded at the rabbit cardiac apex, with spiral fiber structure. The first frame is 1 ms after stimulus ends. Top: Circular wave front propagation measured optically. Bottom: Dipolar stimulus and propagation patterns measured magnetically. The circular wave front contour is overlaid on the respective magnetic data.

The V_m images in Figure 29 demonstrate circular wave front propagation that is similar to the results expected from a simple model of spiral fiber structure. The B_z field, however, shows a broad dipolar pattern associated with the stimulus current (1 ms) , followed by a more localized dipolar pattern of opposite polarity that expands with time (5 – 13 ms). The contour of the V_m wave front is overlaid onto the B_z color map.

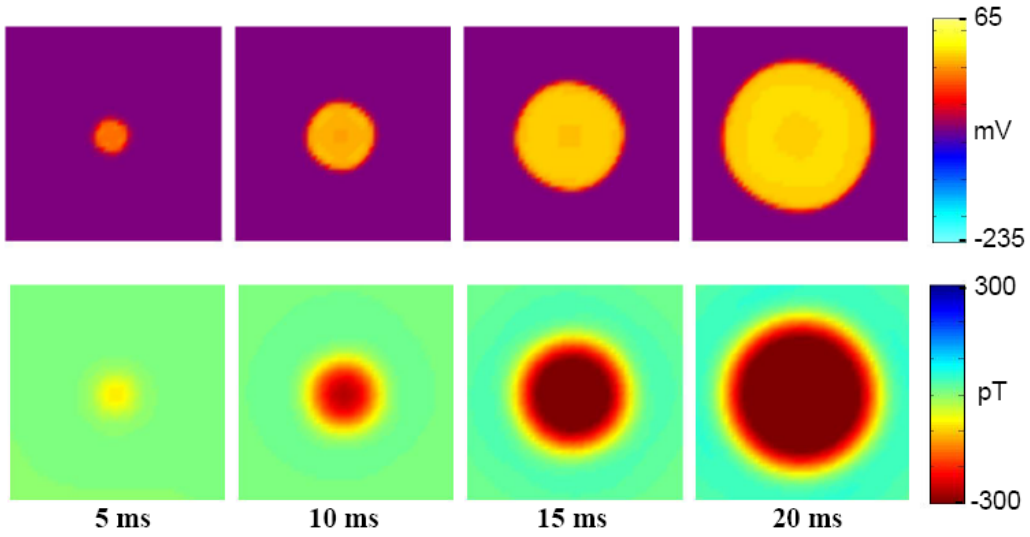

Figure 30 Bidomain model of concentric apex tissue is 10 mm by 10 mm with 1mm depth. Top: Circular wave front propagation. Bottom: Circular magnetic pattern associated with electrical signal.

The monodomain and bidomain models were then used to determine the origin of the observed data. By changing stimulus and spiral orientation parameters in these models, the experimental data could more easily be explained. Figure 28 shows the B_z field produced by a stack of 10 vertically aligned rings of current dipoles in the monodomain model. This shows the predicted circular B_z pattern as expected with a simple model with spiral fiber orientation. In addition, the bidomain model for a vertically aligned stack of a logarithmic spiral bidomain tissue demonstrated this pattern (see Figure 30). The top row of Figure 30 shows the V_m wave front propagation, while the bottom row shows the B_z field from the action current propagation during the respective time step. Both rows demonstrate the circular propagation pattern associated with the spiral tissue symmetry.

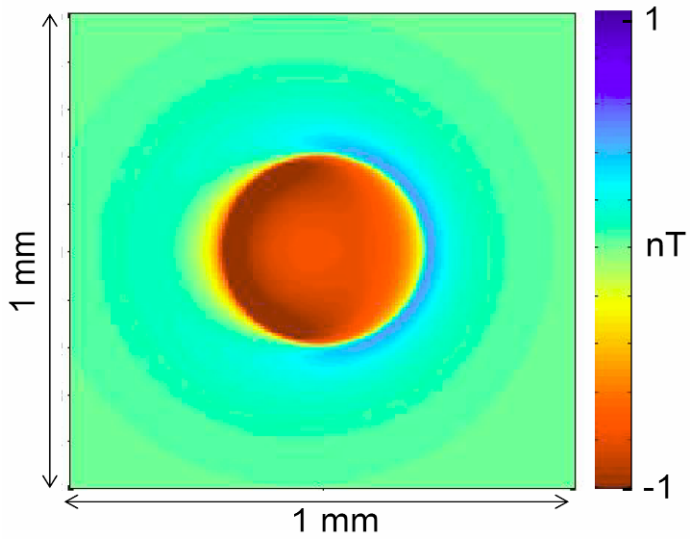

Figure 31 Monodomain model of magnetic field of shifted stack of current dipole rings. The total shift is 0.36 mm.

The results most similar to the experimental data are from a skewed stack of apical tissue in which each layer is shifted laterally by 0.1 mm from the one above. Figure 31 shows a monodomain model B_z calculation of a skewed stack of current dipole rings. Careful examination of the image from this monodomain model reveals a dipole-like B_z image. By moving to a bidomain model, an even more obvious dipole-like characteristic was found. Figure 32 shows a comparison of the experimental versus bidomain model data of a skewed stack of slabs of logarithmic-spiral apex tissue, with Figure 32c indicating the direction of the skew to this stack. On the epicardium closest to the plane where B_z is imaged, the apex center is to the right of the center of the image, and it has shifted to the left of the center of the image by the lowest, endocardial layer. The total shift from epicardium to endocardium is 1 mm. In Figure 32b the V_m wave front propagation is shown in the first row and B_z images in the second row. The time steps start at the beginning of the 4 ms cathodal stimulus and the time continues to show every 2 ms. As the wave front propagates, the circular wave front is shown, similar to the

experimental data in 32a and as expected. The B_z patterns, however, look remarkably similar to the experimental data. There is a dipolar stimulation response that then reverses polarity as the smaller dipolar patterns expand in time.

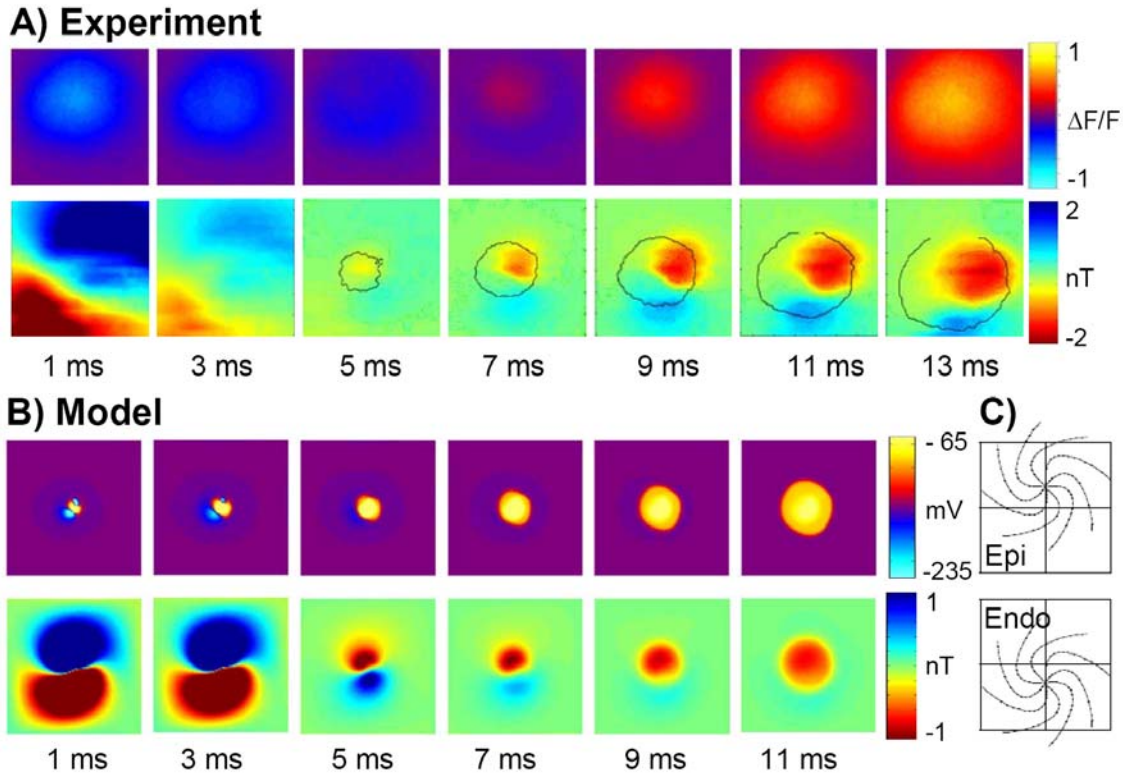

Figure 32 a) Experimental data from the cardiac apex. Top row: Circular wave front propagation. Bottom row: Dipolar magnetic pattern of stimulation and propagation. b) Bidomain model of a skewed stack of apex tissue. Top row: Circular wave front propagation. Bottom row: Dipolar magnetic pattern of stimulation and propagation. c) Skewed stack shift from epicardium to endocardium with the apex at center. The total shift is 1 mm.

Conclusion

For stimulation at the cardiac apex, we expected that the spiral fiber architecture would produce circular patterns for both V_m and B_z. While our optical measurements of V_m wave front propagation were consistent with this, our SQUID microscope measurements of the B_z field from the action currents revealed a more complex B_z pattern than expected. The pattern was consistent with a tilted axis for the apex spiral. We used a

monodomain model of the cardiac apex to calculate B_z and a bidomain model to calculate both V_m wave front propagation and the corresponding B_z field from the stimulation and propagating action currents. When we modeled the apex with a simple, vertically aligned spiral structure, we observed circular wave front patterns for V_m and a similar circular pattern in the B_z field from circular action currents. The skewed stack of rings of current dipoles in the monodomain model demonstrated patterns similar to those from the bidomain model of a skewed stack of spiraled cardiac tissue that stimulated the apex. Because the electrical component of the apex remained as circular wave front propagation while the magnetic data showed dipolar images, electric field measurements alone may not determine the extent of diagnostic information that could be found. Furthermore, this suggests that spiral complexity of the apex has more information that could not be detected with ECG recordings due to electrically silent circular currents. This experiment provides further evidence that the ability of the MCG to measure electrically silent currents might provide useful complement electric measurements.

Future Studies

Our apical studies suggest further improvements in experimental methods. It would be very useful for the measurements of the ECG and MCG to occur simultaneously. This would help eliminate movement in transfer of the heart from optical to magnetic measurements. There is also a need to align the optical and magnetic data with even more precision. The fact that the axis of rotational symmetry from the epicardium to the endocardium is not perpendicular to the epicardial surface may limit our ability to decipher which signal comes from the radial electrical propagation versus

the circular electrical propagation; it may be possible to address this with careful cryoablation of the endocardial apical tissue.

Our data strengthen the case for the existence of new information in the magnetocardiogram. It remains to be seen whether these experiments will inspire further development in MCG imaging to complement ECG measurements, and improvements in the clinical diagnosis of a patient's heart. In order for medical practice to benefit from this new information, it would be extremely helpful to determine a way to separate the contributions from the electrically silent currents from those of the non-silent currents. The first step may be quantitative analysis of high resolution maps of the ECG and MCG.

CHAPTER IV

HIGH-RESOLUTION ROOM-TEMPERATURE SAMPLE SCANNING SUPERCONDUCTING QUANTUM INTERFERENCE DEVICE MICROSCOPE CONFIGURABLE FOR GEOLOGICAL AND BIOMAGNETIC APPLICATIONS

Luis E. Fong, Jenny R. Holzer, Krista McBride, Eduardo A. Lima, Masoud Radparvar, Franz Baudenbacher

Department of Physics and Astronomy
Department of Biomedical Engineering
Vanderbilt University , Nashville, TN, 37235

Hypress Inc., Elmsford, NY, 10523

Adapted from:
L.E. Fong, J.R. Holzer, K. McBride, E.A. Lima, M. Radparvar, F. Baudenbacher, *Review of Scientific Instruments*
Vol. 76, No. 5, 053704

Abstract

We have developed a scanning superconducting quantum interference device (SQUID) microscope system with interchangeable sensor configurations for imaging magnetic fields of room-temperature (RT) samples with sub-millimeter resolution. The low-critical-temperature (*Tc*) niobium-based SQUID sensors are mounted on the tip of a sapphire rod and thermally anchored to the helium reservoir inside the vacuum space of a cryostat. A 25 μm sapphire window separates the vacuum space from the RT sample. A positioning mechanism allows us to adjust the sample-to-sensor spacing from the top of the Dewar. We achieved a sensor-to-sample spacing of 100 μm, which could be maintained for periods of up to 4 weeks. Different SQUID sensor designs are necessary to achieve the best combination of spatial resolution and field sensitivity for a given source configuration. For imaging thin sections of geological samples, we used a custom-designed monolithic low-*Tc* niobium bare SQUID sensor, with an effective diameter of 80 μm, and achieved a field sensitivity of 1.5 $pT/Hz^{1/2}$ and a magnetic moment sensitivity of 5.4×10^{-18} $Am^2/Hz^{1/2}$ at a sensor-to-sample spacing of 100 μm in the white noise region for frequencies above 100 Hz. Imaging action currents in cardiac tissue requires a higher field sensitivity, which can only be achieved by compromising spatial resolution. We developed a monolithic low-*Tc* niobium multiloop SQUID sensor, with sensor sizes ranging from 250 μm to 1 mm, and achieved sensitivities of 480 – 180 $fT/Hz^{1/2}$ in the white noise region for frequencies above 100 Hz, respectively. For all sensor configurations, the spatial resolution was comparable to the effective diameter and limited by the sensor-to-sample spacing. Spatial registration allowed us to compare high-resolution images of magnetic fields associated with action currents and optical

recordings of transmembrane potentials to study the bidomain nature of cardiac tissue or to match petrography to magnetic field maps in thin sections of geological samples.

Introduction

Room-temperature (RT) sample scanning superconducting quantum interference device (SQUID) microscopy (SSM) is a very powerful and promising technique for imaging magnetic field distributions [22,30]. In addition to the SQUID's unsurpassed field sensitivity, this technique is completely non-invasive and can be implemented to study a great variety of samples. RT sample SSM is continuing to play an important role in biomagnetism[1,103-107], non-destructive evaluation [103,108-112] and geomagnetism [113,114].

Since the field and spatial resolution are highly diminished as the distance between the sample and the sensor increases, the key to this technique is to bring the sensor, held at cryogenic temperatures, as close as possible to the sample. It has been shown that the best combination of spatial resolution and field sensitivity for a specific SQUID geometry occurs when the diameter of the pickup coil is approximately equal to the sample-to-sensor distance [115].

A SQUID sensor measures the integrated magnetic flux over the sensing area. Thus, the SQUID's sensitivity to magnetic fields scales as $1/a^2$, where a is the diameter of the sensing area. The fall-off rate of the magnetic field depends on the type of source. For a current-carrying wire the field scales as $1/r$, and for a magnetic dipole it scales as $1/r^3$, where r is the distance from the source. The best combination of field sensitivity and spatial resolution requires $a = r$. It is easy to show that the signal-to-noise ratio of fields generated by a current-carrying wire is proportional to a and for a magnetic

dipole, proportional to $1/a$. Therefore, we have to use different strategies to optimize the sensor geometry and the sample-to-sensor distance depending on the application. In geomagnetism we are dealing with magnetic dipoles, while biomagnetic signals are typically generated by either axial currents or sheets of current.

In this article, we describe a high-resolution SQUID imaging system that can be configured either with monolithic low-*Tc* directly coupled single turn SQUIDs, multiloop SQUIDs, or miniature pickup coils inductively coupled to commercial low-*Tc* SQUIDs, as sensing elements for different applications. The system is highly stable, user friendly and cost efficient. The system versatility is demonstrated by presenting data on high-resolution magnetic imaging of geological thin sections and magnetic mapping of action current distributions in cardiac tissue.

Scanning SQUID microscope system design

In the following sections, we present various designs for directly coupled monolithic SQUID sensors, targeting spatial resolutions ranging from 50 μm to 1 mm, their device characteristics, and their incorporation into our SQUID microscope. We also describe a positioning mechanism, which allows the cryogenic sensors to be positioned within 10 μm of a RT sapphire window, and our Dewar design which allows operation of the SQUID microscope with a helium consumption of 1.0 *l*/day.

Directly coupled monolithic SQUID sensors

Our first generation of SQUID microscopes used hand-wound superconducting niobium-wire miniature pickup coils connected directly to the terminals of a flux

transformer circuit of commercially available low-*Tc* SQUID sensors [116]. With this configuration, we achieved field sensitivities, for frequencies above 1 Hz, of 850 fT/Hz$^{1/2}$ and 330 fT/Hz$^{1/2}$, using a 10-turn 250 μm diameter and a 20-turn 500 μm diameter pickup coil, respectively. However, the miniature pickup coil configuration has two major drawbacks in accomplishing the optimum combination of field sensitivity and spatial resolution. The first limitation is the impedance mismatch between the pickup coil and the flux transformer circuit. For optimum coupling, and therefore, the best possible magnetic field sensitivity, the flux transformer input coil and the pickup coil impedances must be the same. Commercially available low-*Tc* SQUID sensors typically have input coil impedances on the order of 2 μH, which is 20 times higher than the impedance of a 20-turn 500 μm pickup coil. Impedance matching is increasingly difficult as we reduce the pickup coil size and is impractical for spatial resolutions below 250 μm. The second limitation is the spatial integration of the magnetic field over the volume of the pickup coil. For example, a 20-turn double layer cylindrical coil wound with a 25 μm wire has a minimal height of 250 μm. The taller the pickup coil, the less magnetic flux each turn collects, since the magnetic field decays as we increase the distance from the sample. This integration generally compromises the spatial resolution but leads to higher field sensitivity. However, in terms of sensitivity to dipole moments, a better signal to noise ratio can be achieved if a small coil is brought closer to the sample [117]. In this case, the limiting factor is generally the distance between the sample and the SQUID sensor.

To overcome these drawbacks, we developed different types of thin film monolithic low-*Tc* niobium SQUID sensors, which measure the magnetic field coupled directly into the self inductance of the SQUID. In the first type of sensor, a single SQUID

washer acts as the sensing area. Detailed images and an equivalent circuit of this design are shown in Figure 33. In this approach, the sensing area is a two dimensional plane rather than a volume, as in the case of the miniature hand-wound pickup coils. The noise performance of an optimized SQUID sensor is limited by its inductance and is described by the power spectral density of the equivalent flux noise [118]:

$$S_{\phi}(f) = \frac{16 k_B T L^2}{R_n} \tag{17}$$

where f denotes the frequency, k_B the Boltzmann constant, T the operational temperature, R_n the shunt resistance and L the inductance of the device. The main contribution to the inductance is determined by the sensor size [119]. Therefore, the intrinsic noise of the bare SQUID increases with its geometrical size, so this approach cannot be scaled up to sensor diameters larger than 250 μm [10].

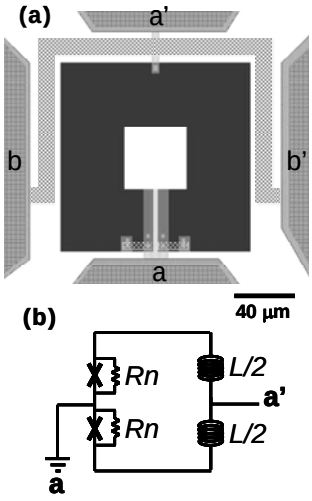

Figure 33 (a) Layout of our bare SQUID design. The SQUID terminals are labeled *a* and *a'* and the contact pads for the feedback coil *b* and *b'*. (b) Equivalent electric circuit diagram of the bare SQUID. *Rn* is the shunt resistance in parallel with the Josephson Junctions and *L* is the inductance of the device.

Using a bare SQUID with a 40 μm hole and a 120 μm square washer, we achieved a flux noise of 4 $\mu\phi_o/Hz^{1/2}$, where ϕ_0 is the magnetic flux quantum, and an equivalent field sensitivity of 1.5 $pT/Hz^{1/2}$ in the white noise region for frequencies above 100 Hz. The bare SQUID design is particularly suited for localized source configurations where the signal decreases rapidly with distance, as is the case for dipolar sources. As we mentioned before, the size of the SQUID washer should be chosen to be comparable to the sensor-to-sample distance for optimum tradeoff between spatial resolution and field sensitivity. The use of the bare SQUID for RT sample SSM is suited for spatial resolutions on the order of tens of microns to 250 μm.

For imaging applications where higher field sensitivities are required, we have to compromise spatial resolution in order to achieve larger effective areas. This is especially true in the case of imaging weak magnetic fields generated by distributed action currents associated with bioelectric phenomena. As we have outlined above, the size of the SQUID sensing area cannot be scaled up by using a bare SQUID design. Therefore, in order to overcome these limitations, we used a monolithic low-*Tc* niobium multiloop, or fractional turn, SQUID design. This approach was first implemented by Zimmerman in 1971 [120]. Figure 34 shows the sensor layout and equivalent circuit of one of our designs. The multiloop SQUID is comprised of multiple pickup coils connected in parallel, thereby reducing the self inductance of the SQUID sensor. In this way, the effective sensing area can be increased with little compromise of field sensitivity. Therefore, we have fabricated a series of multiloop SQUID sensors with diameters ranging from 250 μm to 1 mm. For a 250 μm diameter, 5-spoke multiloop SQUID, we achieved a flux noise of 1.7 $\mu\phi_o/Hz^{1/2}$ with an equivalent field sensitivity of 450 $fT/Hz^{1/2}$ in the white

noise region for frequencies above 100 Hz [121]. For a larger diameter, we increased the number of spokes. Using a 500 μm, 6-spoke multiloop SQUID, we achieved a flux noise of 4.4 $\mu\phi_o/Hz^{1/2}$ with an equivalent field sensitivity of 240 $fT/Hz^{1/2}$ in the white noise region for frequencies above 100 Hz. The increased field sensitivity of the multiloop SQUID design makes it ideally suited for imaging magnetic fields associated with action current propagation in isolated tissue preparations. In comparison with the 250 μm miniature pickup coils, the field sensitivity is improved by a factor of two. Furthermore, by reducing the sensing volume to a single plane, we increased our signal-to-noise ratio and our spatial resolution. Table 3 summarizes the performance of our different sensing configurations. $S_\phi^{1/2}(f)$ and $S_B^{1/2}(f)$ are the magnetic flux and field noise per unit bandwidth at the specified frequency.

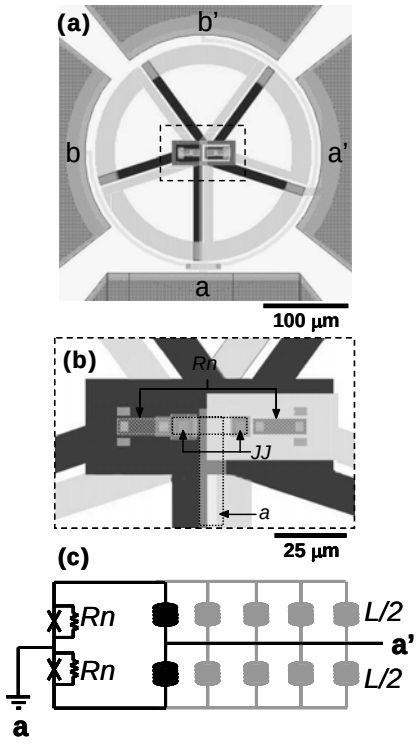

Figure 34 (a) Layout of our multiloop SQUID design. *a* and *a'* are the SQUID terminals and *b* and *b'* the contact pads of the integrated feedback coil. (b) Expanded view of the center of the multiloop SQUID. The Josephson Junctions are labeled *JJ*, the shunt resistances *Rn* and the SQUID upper contacts *a*, respectively. The dark and light regions represent the two superconducting layers forming each spoke, which are separated by an insulating layer in cross over regions. (c) Equivalent circuit diagram of the multiloop SQUID. *Rn* represents the shunt resistance in parallel with the *JJ* and *L* is the inductance of each individual spoke (fractional turn). The inductance of the device is inversely proportional to the number of spokes.

Table 3 Flux noise and field sensitivity of all our SQUID sensor configurations.

Sensor Configuration	$S\phi^{1/2}$ (100Hz) ($\mu\phi_o/Hz^{1/2}$)	$S_B^{1/2}$ (1Hz) ($pT/Hz^{1/2}$)	$S_B^{1/2}$ (100Hz) ($pT/Hz^{1/2}$)	$S_B^{1/2}$ (1KHz) ($pT/Hz^{1/2}$)
Bare SQUID 40 μm washer 40 μm hole	4.0	3.5	1.52	1.50
Multiloop SQUID 250 μm diameter 5 spokes	1.7	2.1	0.48	0.45
Multiloop SQUID 500 μm diameter 6 spokes	4.4	1.85	0.28	0.24
Multiloop SQUID 1 mm diameter 8 spokes	6.0	0.94	0.18	0.15
Miniature coils 250 μm diameter 10 turns	2.0	0.85	0.85	0.85
Miniature coils 500 μm diameter 20 turns	2.0	0.33	0.33	0.33

Cryogenic design

The SQUID Dewar provides the cryogenic temperatures and the thermal insulation which allows for operating a low-*Tc* SQUID in close proximity to a RT sample. A schematic of the SQUID Dewar is shown in Figure 35. The cryogenic system is based on a commercially available custom built G-10 fiberglass Dewar (Infrared Laboratories, HDL-8). In order to achieve liquid He and N_2 hold times of three days, we used 4.96 *l* He and 5.88 *l* N_2 reservoirs in our Dewar. The N_2 reservoir is stacked over the He reservoir. An aluminum thermal radiation shield is thermally anchored to the N_2 reservoir. The radiation shield surrounds the He reservoir and extends to the tail of the Dewar [see Figure 35 (Top)]. The aluminum shielding is wrapped with several layers of aluminized Mylar foil. This reduces the radiation load from room temperature, therefore decreasing both the liquid He and N_2 consumption. This design results in He and N_2 consumption rates of 500 and 1100 standard cubic centimeters per minute (sccm), respectively. The consumption rates are monitored for diagnostic purposes during operation using a mass flow meter.

The RT sample and the vacuum space of the Dewar are separated by a 25 μm thick sapphire window. Several scanning SQUID microscope systems, using mainly high-*Tc* superconducting SQUID sensors, have successfully used this approach for the vacuum window [116,122-124]. Sapphire has a low electrical conductivity which is critical in order to avoid sources of Johnson noise close to the sensor. It also has a high elastic modulus, which minimizes the inward deflection of the sapphire due to the pressure difference. Furthermore, sapphire has the advantage of being optically transparent, which facilitates the centering and alignment procedure of the sensor with respect the window.

A 1 mm thick sapphire backing window with an outer diameter of 25 mm and inner diameter of 1.5 mm supports the 25 μm thin window to minimize bowing. Following the calculations of Lee et al [122], we have estimated a window bowing on the order of 1 μm.

In order to maintain a good insulation vacuum for longer periods of time and to increase the pumping speeds for water and gases like O_2, N_2, and He, we have incorporated a container filled with activated charcoal, which acts as a cryopump. The container is thermally anchored to the He tank. Figure 35 (Bottom) shows its location on the He reservoir.

Our SQUID microscope system can be kept at cryogenic temperatures for periods of over one month without deterioration in performance. During this time range, we performed consecutive 23 hour high-resolution magnetic field scans of geological samples during a demagnetization experiment at a sensor-to-sample distance of 120 μm. The scans were interrupted only by the liquid N_2 and He transfers. Therefore, we confirmed the reliability of the instrument to operate under the identical conditions over long periods of time.

Cold finger design

SQUID microscopes generally have the position of the sensor or pickup coil fixed and it is necessary to adjust the Dewar tail to bring the window as close as possible to the cold sensor. In our experience, this procedure is cumbersome, because not only the distance has to be adjusted but also the tilt between the window and the sensor surface. To overcome part of the problem, we have incorporated a flexure bearing mechanism actuated by a lever arm to precisely and easily control the vertical position of the sensor

into our system. A cross section of the Dewar tail with the lever mechanism is shown in Figure 36 (Bottom). The cryogenic positioning system consists of three different main components. On the top of the Dewar a rotary vacuum feed-through is connected to a G-10 rod. The G-10 rod is attached to a lead screw and a slider which converts the screw rotational movement into a vertical displacement. The slider is connected to the lever arm via a Kevlar tread [see Figure 36 (Middle)]. The lever arm pushes against a shaft that is mounted in the center of two flexure bearings, which are spaced 50 mm apart and anchored to an aluminum support structure. The cold finger is clamped to the shaft and extends it towards the vacuum window. The two flexure bearings in the support structure provide mechanical stability and ensure precise vertical displacement. We have measured a vertical displacement of about 40 μm per turn of the rotary vacuum feed-through. Using this mechanism, we can precisely control the vertical position of the SQUID sensor with respect to the sapphire window. We generally set the distance between the sensor and the sample by approaching the window until we notice a small increase in the He boil off rate as measured by a mass flow meter. We then confirm the position of the SQUID with respect to the sapphire window with an inverted optical microscope and adjust the tilt, if necessary, after the cool down procedure. Using this approach, we found that the distance between the sensor and the sample can be reproducibly adjusted to 100 μm [10].

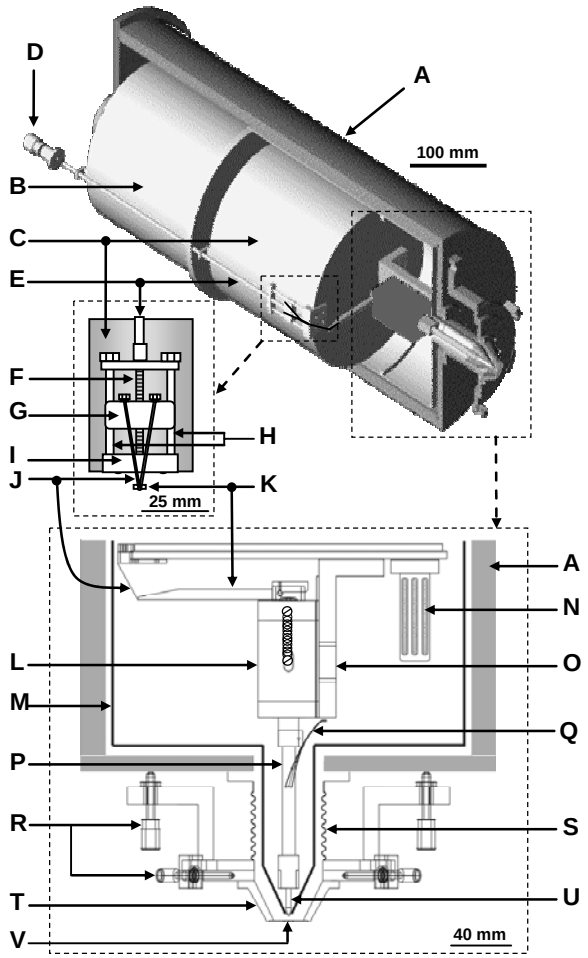

Figure 35 Detailed cross-sectional schematic of the SQUID microscope Dewar. (Top) Cryostat (A) G-10 fiberglass Dewar casing, (B) Liquid N2 reservoir, (C) Liquid He reservoir. (Middle) Positioning mechanism . (D) Rotary vacuum feed-through, (E) G-10 rod, (F) Lead screw, (G) Slider, (H) Slider posts, (I) Brass connection, (J) Kevlar tread, (K) Lever arm. (Bottom) SQUID Dewar tail. (L) Aluminum flexure bearing support structure, (M) Aluminum thermal radiation shield, (N) Cryopump, (O) Copper L-shaped bracket, (P) Copper cold finger, (Q) Flexible copper braids, (R) Micrometer positioning screws, (S) Brass bellows, (T) G-10 cone, (U) Sapphire rod, (V) 25 mm thick sapphire window.

The cold finger terminates in a collet which holds a sapphire rod. The collet is tightened using a G10-nut. A thin layer of Apiezon grease on the sapphire rod provides a good thermal contact to the copper cold finger. Additional thermal links to the solid copper L-shaped bracket mounted on the He reservoir are provided by two flexible copper braids soldered into the center of the cold finger. Depending on the sensor

configuration, the sapphire rod has a bobbin machined at the tip (for miniature pickup coils) or is conical shaped (for monolithic sensor chips).

The monolithic SQUID sensor chips are mounted on the tip of the conical shaped sapphire rod. Using a diamond impregnated wire saw, we first cut the edges of the 2.5 × 2.5 mm^2 chip to reduce its diameter to a few hundred microns. This method is very effective in reducing the size of the chip without damaging the gold contact pads that will be used to connect to the SQUID and the integrated feedback line. Then, we mount the SQUID chip on the tip of the sapphire rod using a low-temperature epoxy resin (Stycast). After mounting the chip, we grind and polish the edges of the chip to reduce its diameter and provide a smooth surface around the edge. We deposited 200 nm silver pads to extend the electrical connection around the edges toward the side of the chip. Four 25 μm gold wires are then attached to the silver pads on the sides of the SQUID chip using silver epoxy to connect the SQUID to a cold step-up transformer, the DC bias source and the feedback coil of the Flux-Locked Loop (FLL) electronics.

System integration

Figure 36 shows a picture of the entire system. The SQUID microscope Dewar is supported by a wooden structure above the non-magnetic scanning stage. Two high-precision piezoelectric inchworm motors are used to perform the XY-raster scan [116]. The whole system is housed in a three layer, μ-metal shielded room (Vacuumschmelze, Hanau) to eliminate near zero and high frequency background noise. The monolithic DC-SQUID sensors are operated in FLL configuration with custom designed electronics [125], which use a flux modulation frequency of 100 KHz. For a high-sensitivity setup, we

typically adjust the feedback resistor to provide a dynamic range of $\pm 10\phi_0$, where ϕ_0 is the flux quantum. The output voltage is digitized by a PCI-MIO card (National Instruments) with 16-bit resolution. The stage and acquisition parameters are controlled by software developed using LabVIEW (National Instruments).

Figure 36 Photograph of the entire system including a non-magnetic scanning stage and SQUID Dewar wooden support structure. The SQUID microscope system is housed inside a 3 layer μ-metal magnetically shielded room.

Measurements and applications

In the following sections, we present applications in two areas where our SQUID microscope system leads to new information difficult to obtain with other techniques. As we outlined above, our system can be equipped with different SQUID sensors depending on the particular magnetic source configuration. We first describe applications using SQUID sensors to image magnetic field originating from magnetizations in geological samples, which do not require a compromise between spatial resolution and field sensitivity, provided we can get the sensor close to the sample. Therefore, a monolithic bare SQUID design is the best suited approach. In contrast, when imaging action or

injury currents generated by living tissue, the current sources are weak and distributed, requiring sensors with higher sensitivities. In order to achieve these higher sensitivities, we must compromise spatial resolution. The multiloop SQUID sensor is ideal for this application.

Paleomagnetism

One of the major research areas that will benefit from the development of our SQUID microscopes is paleo- and geomagnetism. Kirschvink argued that the many paleomagnetic studies were limited by the sensitivity of current magnetometer systems in use [126]. He showed that magnetizations at the level of 10^{-14} to 10^{-15} Am^2 can be preserved in sedimentary rocks. Current commercially available magnetometers like the 2G Superconducting Rock Magnetometer have moment sensitivities around 10^{-12} Am^2. The sensitivity of our SQUID microscope system can also be expressed as moment sensitivity. For our bare SQUID design with an effective diameter of 80 μm, we calculated a magnetic moment sensitivity of 5.4×10^{-18} $Am^2/Hz^{1/2}$ for frequencies above 100 Hz at a sensor-to-sample spacing of 100 μm.

Superconducting Rock Magnetometers measure the average magnetization in a sensing volume of a 1 in round and 1 in high cylinder. In contrast, SQUID microscopy provides images of the magnetic field above the sample with sub-millimeter resolution. This is especially important for geological samples which are not homogeneously magnetized. We can now study the geomagnetic properties on a grain-by-grain basis in integral geological samples in massively parallel measurements. This results in

information which is difficult or impossible to obtain using conventional superconducting rock magnetometers.

Using our first generation SQUID microscope with a 250 μm pickup coil, we imaged the magnetic field associated with the remanent magnetization of the Martian meteorite ALH84001. We performed a thermal demagnetization experiment to determine the maximum temperature the rock has been exposed to since ejected from Mars through a meteoroid impact [127,128]. Since then, we have improved the SQUID microscope, and incorporated our monolithic bare SQUID sensors, which drastically improved the field sensitivity and spatial resolution of the system. Figure 37 shows a direct comparison between images obtained with a 250 μm pickup coil and a bare SQUID washer design with an effective diameter of 120 μm. The images show magnetic field distributions resulting from the remanent magnetization of a 30 μm thin section of a basalt pillow from the Kilauea Volcano, Hawaii at a sample-to-sensor distance of 120 μm. In order to show the improvement in spatial resolution, we took a line scan along identical features at the same location in both magnetic images [see Figure 37 (d)]. The red line is from the scan measured with the 250 μm pickup coil and the blue line from the bare SQUID with an effective diameter of 120 μm. We can clearly identify smaller features on the order of the effective diameter of the monolithic SQUID sensor, which are averaged in images obtained with the 250 μm pickup coil. The spatial averaging has both contributions from the larger diameter and the volume of the pickup coil.

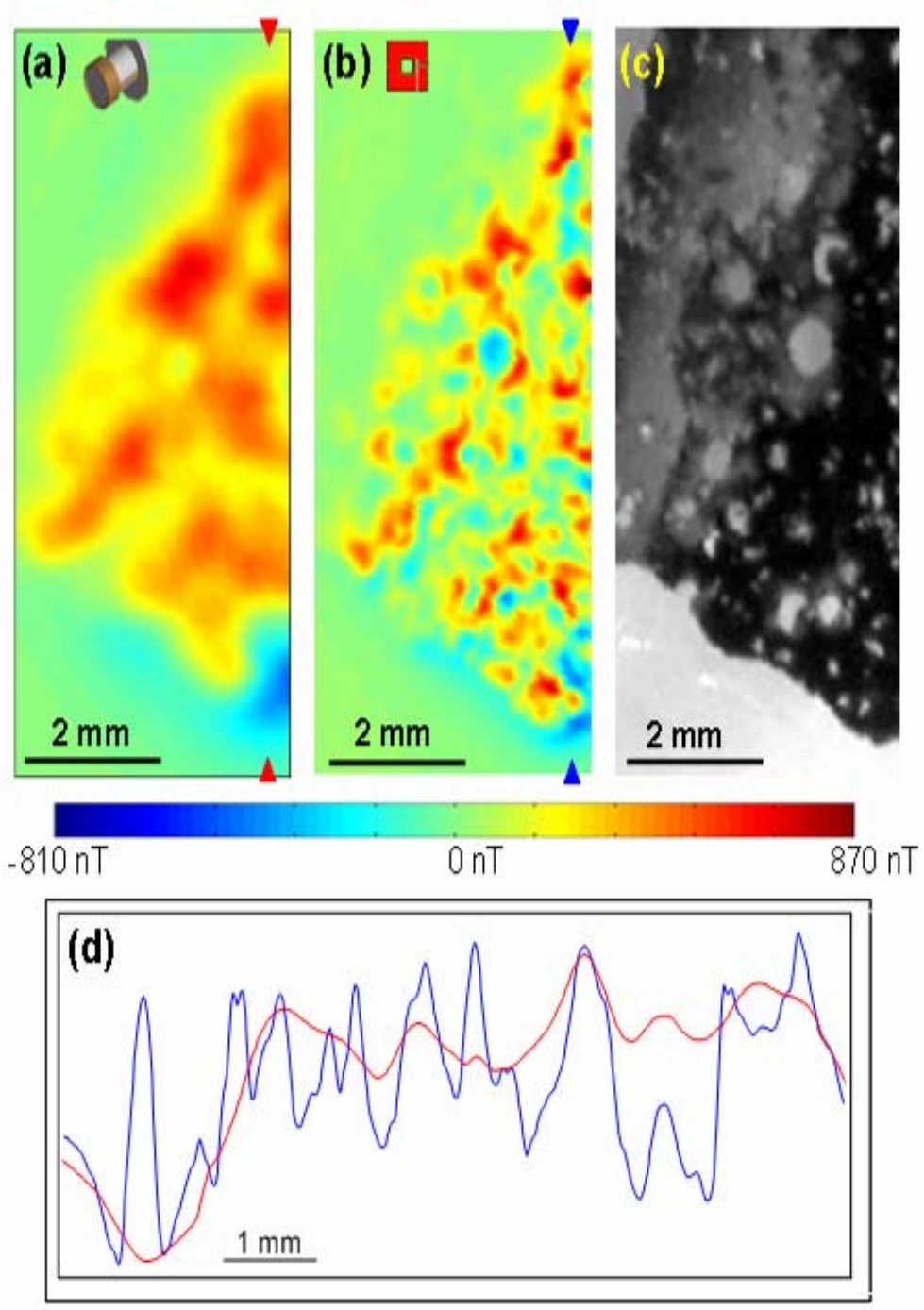

Figure 37 Comparative magnetic field maps of a 30 µm thin section of a basalt pillow recorded using (a) a hand wound 9 turns 250 µm diameter pick up coil inductively coupled to a commercial SQUID sensor, (b) bare SQUID design with an effective diameter of 120 µm. and (c) Optical picture of the imaged area. (d) Line scans through both magnetic field images at identical locations as indicated by arrows in (a) and (b). The red line corresponds to image (a) and the blue line to image (b).

Many paleomagnetic techniques require successive recordings of the magnetic field of the sample after demagnetization or remagnetization experiments. For these experiments it is essential to spatially correlate the magnetic field maps after each recording, which requires the sample to be registered with respect to the sensor height and the scanning directions. To address this issue, we developed a spring-loaded mechanism attached to the scanning stage, which allows us to scan a flat thin section in contact with the sapphire window. Figure 38 shows a schematic of the mechanism. A rectangular Plexiglas sample holder sits over a pair of rubber bands and fits tight inside a square opening. The mechanism is mounted on top of the pedestal of our scanning stage. In this way, we scan a flat sample in contact with the window and guarantee that the sample will be as close as possible to the sensor. This set up allows us to remove the sample, perform Alternating Field (AF) demagnetization or Isothermal Remanent Magnetization (IRM) steps on the sample and place it in the same location to correlate measurements and identify the underlying petrography.

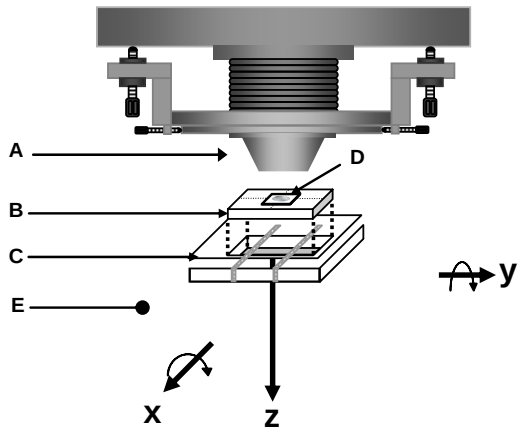

Figure 38 Schematic of spring-loaded mechanism mounted on the top of the scanning stage. (A) Tail of the SQUID microscope, (B) sample holder, (C) support frame (D) rubber bands, (E) geological thin section (sample),(F) Plexiglas pedestal attached to base of the scanning stage.

To test the precision of the spring loaded mechanism, we used a 1 μm precision dial indicator to measure the relative tilt between the surface of the window and a flat sample while scanning. Figure 39 shows this measurement. First, we measured the relative tilt between the scanning stage and the window, Figure 39(a). The two steps in the scan are caused by the thickness of the thin sapphire window with a thin layer of epoxy. Then, we placed the dial indicator below the sample holder in order to measure the tilt of the holder while scanning against the window, Figure 39(b). Comparing these two measurements, we estimated a relative tilt between the surface of the window and the sample holder of 0.097^{o} while performing a scan.

To register the magnetic field images and correlate them to petrography or a compositional analysis we have developed a spatial registration technique. Figure 40 shows an example of the method for a geological thin section. After the sample's magnetic distribution has been acquired, we remove the sample and place a wire in a cross-hair pattern in its place. We then apply an alternating current through the wire and measure its magnetic field pattern using a lock-in amplifier technique over the same area where the sample was located. From the wire magnetic mapping, we can localize the position of the wire by the zero-field crossing. Since both the sample and the wire scan were measured with respect to the same origin defined by the coordinate system of the scanning stage, we can now spatially superimpose these two images. We then take an optical image of the wire pattern and the sample for angular alignment. Using a scale bar we can then adjust the size of the optical image to the magnetic image which was taken using the reference coordinate system of the scanning stage. Using this technique we can overlap and correlate specific features in the magnetic images with the location in the

optical image. This registration technique could also be used for a correlation to a compositional or crystallographic analysis.

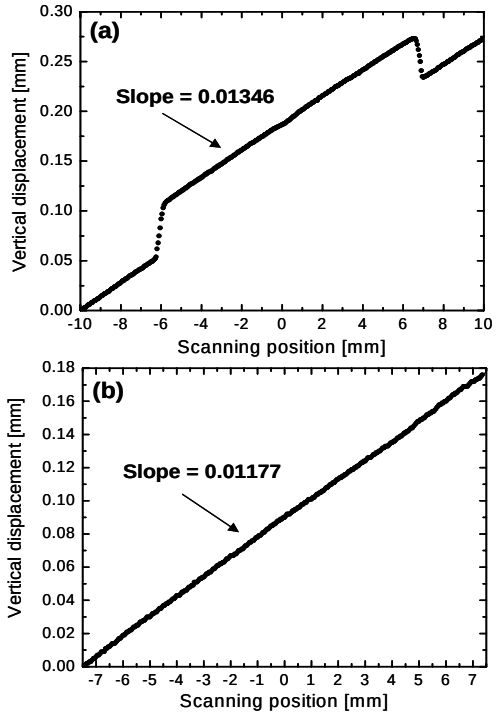

Figure 39 (a) Relative height between the scanning stage platform and the vacuum window of the SQUID microscope during a line scan. The steps in the curve result from the thickness of the 25 μm sapphire window and a thin layer of epoxy used to glue the sapphire window to the backing window. (b) Vertical displacement of the sample holder while pressed against the window by the spring loading mechanism during a line scan. From these measurements, we estimated a tilt of 0.097^{o} between the sample surface and the sapphire window.

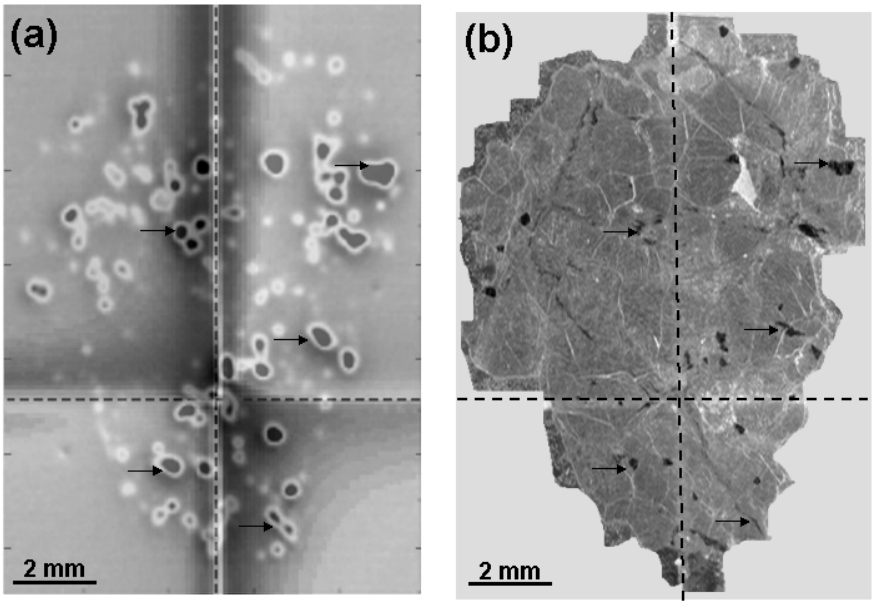

Figure 40 (a) Superposition of the magnetic field map from the sample and the magnetic field generated by wires across the sample used for registration purposes. (b) Optical picture of the sample. The dashed line shows the position of the wire. This registration technique allows us to correlate magnetic features with features in the optical image (arrows).

Our sample-to-sensor spacing of around 100 μm limits both our spatial resolution to 100 μm and our moment sensitivity to 10^{-18} Am^2 /$Hz^{1/2}$ in the white noise region for frequencies above 1 Hz. We are currently working to reduce both the sample-to-sensor spacing and the sensor size. We expect to improve our spatial resolution by at least a factor of two and consequently, our moment sensitivity by a factor of eight.

A great variety of rock- and paleomagnetic experiments can now be done on individual grains in standard petrographic thin sections and the measured magnetic field can be matched to the composition and to the petrography of the sample. The incorporation of monolithic bare SQUID sensors into our scanning SQUID microscope allows measurements currently not possible with existing commercially available instrumentation.

Biomagnetism

SQUID magnetometer systems have been widely used to study a great variety of bioelectric and biomagnetic phenomena [129]. Multichannel SQUID systems with pickup coil diameters of 10 to 30 mm with a similar sample-to-sensor spacing are generally used in human studies. These systems do not provide the spatial resolution necessary to study the generation of the magnetic activity or injury currents at tissue and cellular scales. In excitable tissue extracellular potentials, transmembrane potentials, or action currents are interrelated. To make model predictions, one should at least measure more than one of these quantities, especially in tissues with different anisotropies in the intra- and extracellular space. The extracellular potentials are typically recorded using microneedle arrays. However, the insertion of microneedles influences the measurement results [130] and is impractical to achieve sub-millimeter spatial resolutions. Our approach is to record the transmembrane potential optically and the action currents using SQUID microscopy, which allows us to obtain more detailed information on the generation of the magnetocardiogram (MCG). High-resolution biomagnetic imaging provides insights that will improve existing mathematical models of biological tissue.

By using a 6-spoke 500 μm diameter multiloop SQUID, we recorded magnetocardiograms (MCGs) on the surface of a perfused isolated rabbit heart. Figure 41 shows a photograph of a perfused isolated rabbit heart in a tissue bath under the tail of the Dewar. A bath temperature of 38° C is maintained by a second perfusion system and a heat exchanger. The heart was stimulated at a frequency of 3.33 Hz using a single coaxial electrode placed on the posterior left ventricular (LV) wall. The amplitude of the stimulation pulse was 2 mA, which is just above the threshold for diastolic stimulation.

The anterior depolarization wave fronts generated by the stimulation pulse were imaged using a membrane bound fluorescent dye and a high-speed CCD camera [131]. After recording the transmembrane potential optically, the isolated rabbit heart was positioned under the tail of the SQUID microscope and lightly pressed against the sapphire window to minimize the sample-to-sensor spacing. One-second long time traces of the magnetic field generated by the excitation were recorded at 144 locations on a 12 mm × 12 mm grid with a step size of 1 mm. The data acquisition was triggered on the stimulation pulse, allowing for synchronization of the magnetic field traces to produce a time series of two-dimensional field maps.

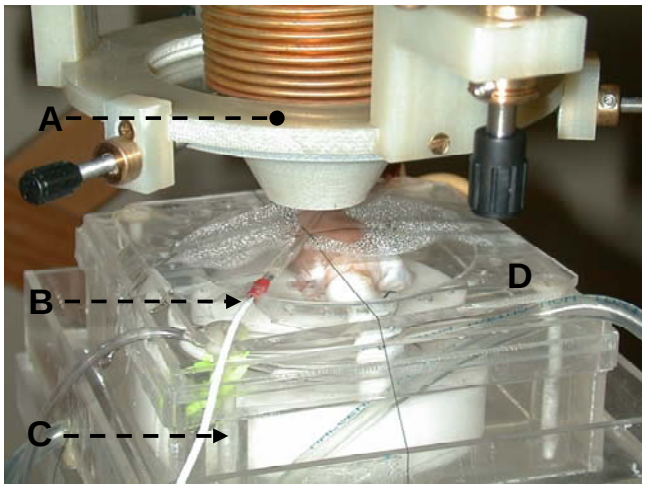

Figure 41 Photograph of the experimental setup to record the magnetocardiogram on the surface of an isolated rabbit heart. (A) Tail of the SQUID microscope, (B) isolated rabbit heart, (C) tissue bath and (D) registration wires.

Figure 42(a) depicts the areas for the optical (blue) and the magnetic (red) recordings in relation to the anatomical features of the isolated heart. Time traces of the transmembrane potential and the magnetic field at the marked location are shown in Figure 42(b). An optical image of the propagating depolarization wave front 53 ms after stimulation can be seen in Figure 42(c). The optical data are offset by the resting potential

and normalized by the maximum amplitude of the transmembrane potential. The wave fronts can be identified as the boarder between depolarized ($V/V_{max} \sim 1$) and resting tissue ($V/V_{max} \sim 0$). As shown in the image, two wave fronts originating from the posterior point stimulus are about to collide. A magnetic field map of an area on the left ventricle, as marked by the white square in Figure 42(c), is shown in Figure 42(d).

In a previous study, we used a line stimulus in close proximity to the imaging area to generate a plane wave. We found that a reversal of magnetic field polarity is associated with the depolarization wave front [132]. The data presented here show that the wave front geometry can not be accurately predicted by a contour line between areas of opposite field polarity. This suggests that action currents flow over larger distances and therefore, the wave fronts influence each other over larger distances than suggested by the depolarization contours of the transmembrane potential maps.

It is clear from our observations that the intra- and interstitial potentials, and therefore, the currents are not scaled versions of the local transmembrane potential. The currents are determined by the transmembrane potential throughout the tissue and a local description in terms of a generator model is not applicable [133,134]. A detailed analysis of the data, a reduction in dimensionality to reduce the influence of fiber orientation, and well-defined wave front geometries are required to make more precise model predictions.

The improvement in field sensitivity achieved by using monolithic multiloop SQUID sensors allows us to study in more detail the relationship between extracellular potentials, transmembrane potentials and action currents, especially in thin layers of connective cardiac or brain tissue. We hope to achieve a higher sensitivity by optimizing the process parameters to lower the critical currents of the Josephson Junction of our

multiloop SQUID sensors. For an optimized 1 mm multiloop SQUID sensor, we expect to achieve field sensitivities on the order of 20 fT/Hz$^{1/2}$.

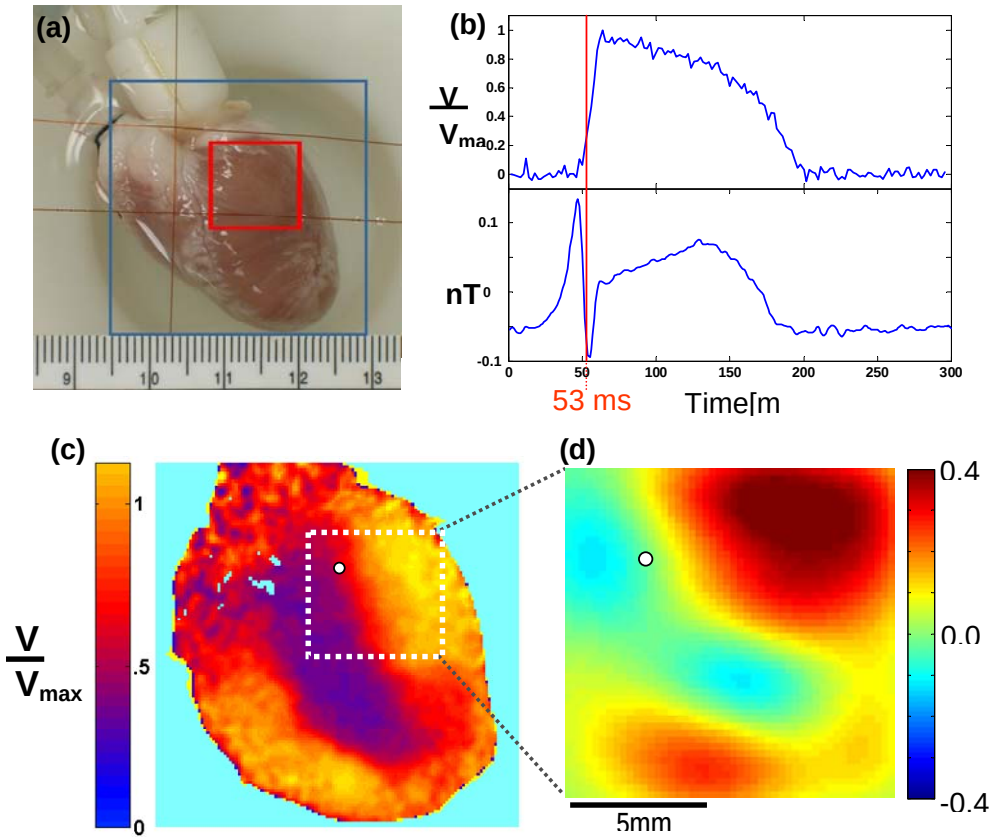

Figure 42 (a) Optical image of a Langendorff perfused rabbit heart indicating the imaging areas used to record transmembrane potentials (blue square) and magnetic fields (red square) associated with action currents. (b) Time trace of the transmembrane potential and the magnetic field recorded from the same location on the surface of the heart. (c) Image of the transmembrane potential distribution 53ms after stimulation. The two wave front from opposite sides are about to collide. (d) Magnetic field image composed of time traces 53 ms after the stimulus from the area indicated by a white dashed square in (c).

Acknowledgments

We would like to thank Ben Weiss, Joseph Kirschvink, and John Wikswo for fruitful discussion. This work was supported in part by NIH Grants (1-R43-RR16157-01 and 2-R01-HL58241-06), NSF – Earth Science (EAR-0004101) and DARPA (DSR # 16966).

CHAPTER V

HIGH RESOLUTION IMAGING OF CARDIAC BIOMAGNETIC FIELDS USING A LOW TRANSITION TEMPERATURE SUPERCONDUCTING QUANTUM INTERFERENCE DEVICE MICROSCOPE

Luis E. Fong, Jenny R. Holzer, Krista McBride, Eduardo A. Lima, Masoud Radparvar, Franz Baudenbacher

Department of Physics and Astronomy
Department of Biomedical Engineering
Vanderbilt University, Nashville, TN, 37235

Hypress Inv. Elmsford, NY, 10523

Adapted from:
L.E. Fong, J.R. Holzer, K. McBride, E.A. Lima, M. Radparvar, F.Baudenbacher, *Applied Physics Letters*
Vol. 84, No.16, pp. 3190 – 33192, April 2004.

Abstract

We have developed a multiloop low-temperature superconducting quantum interference device (SQUID) sensor with a field sensitivity of 450 fT/Hz$^{1/2}$ for imaging biomagnetic fields generated by action currents in cardiac tissue. The sensor has a diameter of 250 μm and can be brought to within 100 μm of a room-temperature sample. Magnetic fields generated by planar excitation waves are associated with a current component parallel to the wave front, in agreement with predictions of the bidomain model. Our findings provide a new basis for interpreting the magnetocardiogram.

Introduction

Superconducting Quantum Interference Device (SQUID) magnetometers have been used successfully to study a wide variety of bioelectric phenomena [129]. Of particular interest are magnetic fields generated by currents in the heart and the brain. Diagnostic multichannel systems detect the magnetic far field outside the body and extrapolate to the source configuration. To address the validity of the source configuration, we have to study the magnetic activity at the tissue level with cellular-scale spatial resolution [135]. High resolution imaging of biomagnetic fields will ultimately lead to a better understanding of how the magnetocardiogram (MCG) and the magnetoencephalogram (MEG) are generated and their diagnostic value. To attain high spatial resolution, the sensor must be in close proximity to the room-temperature (RT) sample. Even though high transition temperature SQUID microscopes have achieved a sample to sensor distance of 15 μm [105,122], they lack the required field sensitivity to measure the weak magnetic fields due to the distributed sources associated with bioelectric phenomena.

We recently addressed this by using sub-millimeter superconducting pickup coils supported within the vacuum space of a cryostat and coupled to the flux transformer circuit of a commercial SQUID sensor [1,116]. Although this configuration achieved a sample-to-sensor spacing of 100 μm with field sensitivities of 330 fT/Hz$^{1/2}$ for a 500 μm diameter pickup coil with 20 turns, it suffers from two major drawbacks. First, the impedance mismatch between the pick up coil and the flux transformer input coil limits the field sensitivity. Second, the cylindrical pickup coil results in a spatial averaging along the coil axis, degenerating the spatial resolution and reducing the flux due to the decay of the magnetic field with distance from the source.

One approach to overcome these drawbacks is to use Nb thin-film monolithic SQUID sensors and detect the flux induced in the bare SQUID. However, this sensor configuration is limited by small SQUID self inductances and therefore the achievable sensitivity of a few pT/Hz$^{1/2}$ is best suited for high-resolution imaging of magnetic dipole sources. In order to increase the field sensitivity further, one has to sacrifice spatial resolution and increase the effective area without increasing the inductance of the SQUID. A design, which achieves large effective areas, is a multiloop magnetometer, also known as fractional turn SQUID. This configuration was first introduced by Zimmerman [120], and later adapted by Drung *et al*.[136] who developed monolithic niobium thin-film sensors with 8 mm pickup coils for biomagnetic multichannel systems to record human MCGs and MEGs [137] and 1.5 mm diameter sensors with integrated flux transformer for nuclear magnetic resonance [138,139]. We have adapted this design and fabricated Nb thin film monolithic multiloop SQUID sensors with sub-millimeter

resolutions and field sensitivities < 1 pT/Hz$^{1/2}$, which are ideally suited for imaging biological tissue preparations.

In our approach, we use five input coils (spokes) connected in parallel with the Josephson Junctions (JJ) located in the center of the device forming the SQUID sensor. An image of our sensor is shown in Figure 43. A loop around the device is used to feedback magnetic flux for operation in a flux-locked loop (FLL).

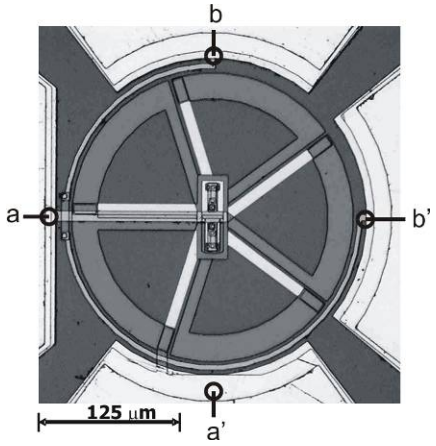

Figure 43 Optical picture of the multiloop magnetometer. The SQUID terminals are labeled a and a' and the integrated feedback terminals b and b'.

The noise performance of a SQUID sensor depends on its total inductance [118], and is given by the power spectral density of the equivalent flux noise:

$$S_\phi(f) = \frac{16 k_B T L^2}{R_n} \tag{18}$$

where f denotes the frequency, k_B the Boltzman constant, T the operational temperature, R_n the shunt resistance and L the inductance of the device. Equation **(18)** is only approximately valid for $\beta_L = 2LI_c/\phi_0$ close to unity and in the limit of small thermal fluctuations both of which conditions apply to our SQUID sensors. I_C denotes the critical current per junction and ϕ_0 the flux quantum. A detailed inductance

calculation of the multiloop SQUID configuration, L, and the geometric effective area, A_{eff}^{*}, are given by[140]

$$L = \frac{L_p}{N^2} + \frac{L_s}{N} + L_j \tag{19}$$

$$A_{eff}^{*} = \frac{A_p}{N} - A_s \tag{20}$$

where L_p and A_p are the inductance and area of the circular coil without spokes, L_s and A_s are the inductance and area of one spoke, L_j is the small parasitic inductance of the Josephson junction connection lines and N the number of spokes. Based on the optimization procedure outlined by Drung *et al.*[140] and calculations by Moya *et al.* [141], we evaluated the field sensitivity for different numbers of spokes and a fixed sensor diameter of 250 μm. The best field sensitivity was achieved with 5 spokes resulting in a total inductance of 24 pH and a geometric effective area of 7.85×10^{-3} mm^2.

The Josephson Junctions (JJs) were fabricated using a Nb/Al0x/Nb trilayer process with Mo thin film shunt resistors. With our photolithographic process, we achieved a JJ size of 2×2 μm^2, a JJ self-capacitance C of 0.6 pF/JJ, and a critical current per junction I_c of 15 μA at a process-specific critical current density of ~100 A/cm^2. The parameters of our device are listed in Table 4 and were taken from both the current-voltage (I-V) and voltage-flux (V-Φ) characteristics at 4.2 K. A_{eff} is the effective sensing area, A_{eff}^{*} is the geometrical area (calculated using equation 6.2), L is the SQUID inductance, I_c is the critical current, R is the shunt resistance per junction, ΔV is the peak-to-peak voltage modulation, $\beta_L = 2LI_c/\Phi_0$ is the reduced inductance parameter.

The noise performance was measured inside a three layer, μ-metal magnetically shielded room by operating the device in the FLL with a modulated flux of 100 kHz and a DC bias current. By using a pair of Helmholtz coils, we applied a homogeneous field which allowed us to determine the effective area, A_{eff}, of 7.86×10^{-3} mm^2, which is in good agreement with the geometrical area, A^*_{eff}.

Table 4 Parameters for a representative multiloop SQUID magnetometer.

A_{eff}	A^*_{eff}	L	I_c	R	ΔV	β_L
[mm^2]	[mm^2]	[pH]	[μA]	[Ω]	[μV]	
$7.85*10^{-3}$	$7.86*10^{-3}$	24.1	15.5	2.2	32.9	0.36

Results

Figure 44 shows both the magnetic field and flux noise power spectral density of our multiloop SQUID for frequencies from 0.1Hz to 1 kHz. The peaks in the spectrum are mainly associated with noise induced through the power supply of the feedback electronics and can be eliminated with tighter specifications. We achieved a magnetic flux noise, $S_\Phi^{1/2}$, of 1.7 μΦo/Hz$^{1/2}$ and an equivalent magnetic field noise, $S_B^{1/2}$, of 450 fT/Hz$^{1/2}$, both in the white noise region. We found that the 1/f noise, which generally appears for frequencies below 1 Hz, begins around 50 Hz. It has been shown that there are two main sources of 1/f noise in DC SQUIDs [142,143]: the motion of flux lines trapped in the body of the SQUID and fluctuations in the JJ critical current. At present, it is not clear which type of these most likely sources are responsible for the observed 1/f noise in our devices. However, we expect the component due to I_C fluctuations to be reduced by implementing a bias current reversal scheme [142].

The multiloop SQUID sensor was incorporated into the vacuum space of our cryostat and brought within 50-100 μm of a 25 μm thick RT sapphire window separating the sample and the vacuum space. Details of the chip mounting procedure, the cryogenic design, the magnetic shielding and the scanning stage are described elsewhere [10,116]. The imaging properties of the sensor have been evaluated using high resolution scans of a 10 μm thin film wire with opposite scan directions. We have found no directional dependence of the image, suggesting isotropic flux collection.

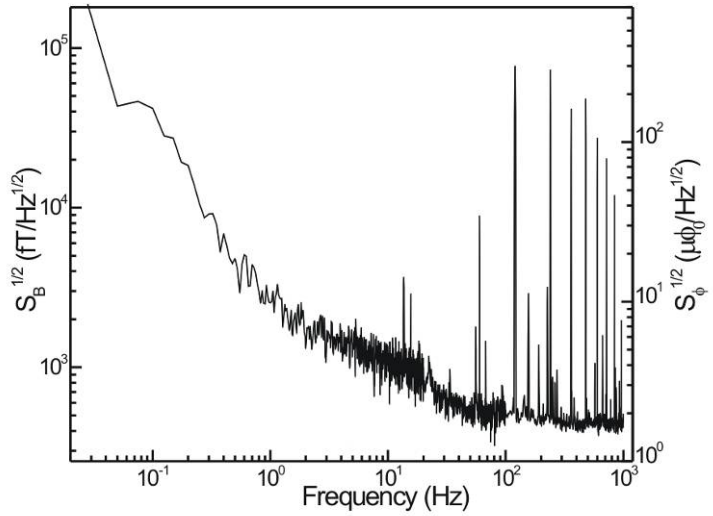

Figure 44 Field noise and flux noise spectral density of our multiloop SQUID magnetometer chip

To investigate the source of the MCG and validate current cardiac models, we mapped the magnetic field associated with planar excitation wave fronts on the left ventricle (LV) of a reversely perfused isolated rabbit heart pressed lightly against the sapphire window of the SQUID microscope. Using a line of three bipolar stimulation electrodes, we induced a propagating planar wave front onto the LV. The wave front geometry and position was confirmed using an optical imaging system and a voltage-

sensitive dye as describe by Lin *et al.*[131] The location of the imaging area and the electrode configuration are shown in Figure 45a.

In order to override the internal pacemaker, we stimulated the heart at frequencies around 3 Hz with current amplitudes of 1-2 mA, which is typically 1.5 times the diastolic stimulation threshold. The stimulation pulse triggers the recording of a MCG. Figure 45a shows a typical MCG time trace (z-component) of three beats recorded with a bandwidth of 0.1 – 100 Hz. The largest peaks are due to the stimulation current and precede the actual heart beats. We estimated a signal-to-noise ratio (SNR) of 10:1 referenced to the amplitude of the heart beats. The SNR can be improved by post processing using a comb filter centered on each harmonic. The first 50 harmonics are isolated in the frequency domain and used to reconstruct the MCG. Figure 45c displays the MCG after signal processing.

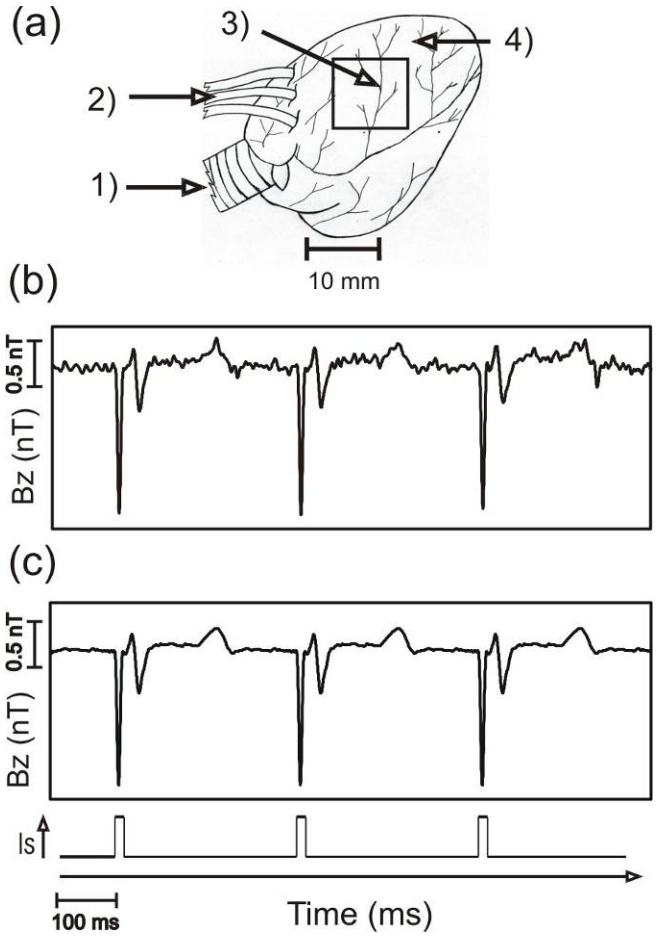

Figure 45 (a) Langendorff-perfused rabbit heart preparation: 1) temperature controlled perfuse inlet, 2) line of three bipolar electrodes, 3) heart's left ventricle (LV), 4) imaging area. MCG recording of three consecutive heart beats. (b) Raw and (c) post processed data. The largest peaks are from the stimulus current and are followed by ventricular depolarization and repolarization signals.

We recorded MCGs at 400 locations on a 10 mm×10 mm grid with a step size of 0.5 mm. Figure 46 shows the magnetic field generated by the excitation wave front 40 ms after the stimulation. The overlaid arrows represent schematically the direction and the amplitude of the action currents generating the magnetic field. The currents were calculated under the assumption of two-dimensional current distribution, as described by Roth *et al*.[144] The leading edge of the excitation wave front can be identified by a reversal of the sign of the magnetic field amplitude. The main component of the corresponding current is parallel to the depolarization wave front, which was confirmed using

membrane bound voltage sensitive fluorescent dyes. This current component can only be explained in the framework of the bidomain model for cardiac tissue. In this model [144,145], cardiac tissue is represented by a three-dimensional electrical cable with distinct intra-cellular and extracellular spaces separated by the cell membrane. The electrical conductivities and their anisotropies in the intra- and extracellular spaces are different. The magnetic field is a superposition from currents in the intra- and extracellular space. Our experiments are the first that demonstrate the importance of the bidomain approach in describing plane wave propagation in cardiac tissue. These observations are a sensitive test of the bidomain model and are in qualitative agreement with theoretical predictions.[146]

In conclusion, we have developed and fabricated monolithic multiloop SQUID sensors with a diameter of 250 μm and a field sensitivity of 450 $fT/Hz^{1/2}$. The SQUID sensor was incorporated in a SQUID microscope and brought within less than 100 μm of the epicardium of isolated rabbit hearts to image the action current distributions of plane waves. We found a current component parallel to the wave front which is in agreement with predictions of the bidomain model. Consequently, the bidomain model should be the basis for forward calculations of the MCG. We anticipate the use of our system to study a wide variety of biomagnetic phenomena at the tissue level.

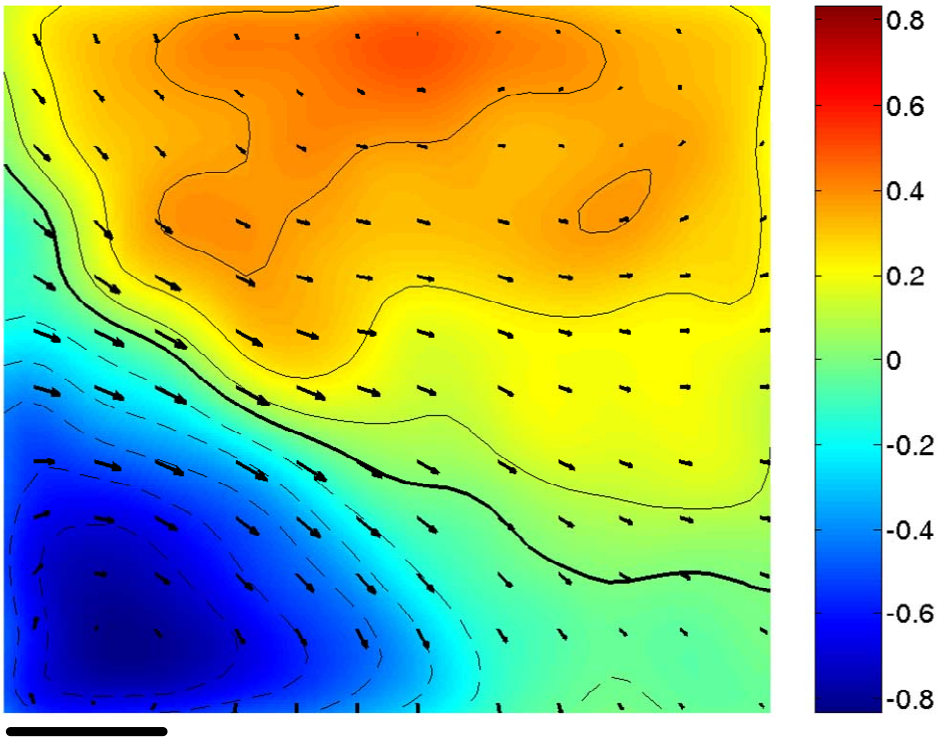

Figure 46 Magnetic field map 40 ms after stimulation with the corresponding isocontour lines, dashed lines represent negative fields, solid lines represent positive fields. The thick line is the zero field contour and is associated with the leading edge of the depolarization wave front. The arrows represent the calculated action current distribution.

Acknowledgments

We thank Venya Siderov and especially John Wikswo for fruitful discussions. The work was partly supported by NIH (1-R43-RR16157-01 and 2-R01-HL58241-06) and NSF – Earth Science (EAR-0004101).

CHAPTER 6

SUMMARY

Summary

The objective of this research project was to study the action currents in the isolated rabbit heart associated with electrical stimulation at the apex using SQUID microscopy and epifluorescent imaging. A parallel project involved the optimization of the SQUID microscope by implementing monolithic bare SQUID chips, which have low noise and high sensitivity, into the microscope.

In review, Chapter 2 discussed the SQUID microscope along with the optimization process for the monolithic and coil-configuration SQUID sensors. With manufacturing help from Hypress, Inc., we have designed new batches of SQUID monolithic chips that have low noise and high spatial resolution. This has improved our SQUID microscope capabilities for spatial measurements, especially in studying rock magnetization.

Chapter 3 discussed the magnetic field distributions found in the cardiac apex of white New Zealand rabbits. This research has allowed us to explore the fact that the spiral structure of the cardiac apex produces electrically silent currents that can be detected through magnetic measurements. We saw that the wave front propagation measurements showed a circular pattern, as expected, but the magnetic field images showed an unexpected dipolar pattern. Through a series of monodomain and bidomain theoretical modeling, we found that the experimental measurements much resembled the models that

used an apex with a tilted axis of rotation. The measured membrane potential and magnetic images show different field patterns, further proving that MCG measurements along with ECG measurements would be complementary to each other in clinical diagnosis of the heart.

In Chapter 4,[12] the SQUID microscope and monolithic chips are discussed further. Magnetic measurements were made using the monolithic bare SQUID sensors on a geological thin sample and the monolithic multiloop SQUID sensor on the left ventricle of a New Zealand rabbit heart. With the monolithic design, we have obtained a more detailed image of the magnetic field associated with the remnant magnetization of the Martian meteorite ALH84001. This was due to the Vanderbilt SQUID sensors' high spatial resolution, which is currently better than that of any commercially available SQUID sensors. The monolithic multiloop SQUID has allowed us to study the relationship between extracellular potentials, transmembrane potentials, and action currents, which will be very useful in future studies of thin layers of connective cardiac or brain tissue. Chapter 5 expanded on the development and use of the monolithic multiloop SQUID, including its use to study the left ventricle's magnetic fields associated with the action currents.[25]

These developments of the SQUID microscope and magnetic cardiac research have advanced magnetic measurement capabilities and provided a better understanding of the action current flow in the heart. We hope that the SQUID can be used to understand more entities in cardiac and bioelectric magnetic fields and become a vital medical diagnostic tool.

APPENDIX A

ABSTRACTS

ULTRA-FINE SCALE MAGNETOSTRATIGRAPHY OF MN CRUST WITH SQUID MICROSCOPE

IROKUNI ODA[1], AKIRA USUI[2], BENJAMIN P. WEISS[3],

FRANZ J. BAUDENBACHER[4], LUIS E. FONG[4], KRISTA K. MCBRIDE[4]

[1]*Geological Survey of Japan, AIST*

[2]*Kochi University*

[3]*Massatusetts Institute of Technology*

[4]*Vanderbilt University*

Asia Oceania Geosciences Society (AOGS), Singapore

2006 Conference

Hydrogenetic Mn crust is considered as a chemical archive, which enables us to reconstruct deep circulation of the ocean. In order to construct a method to give reliable age model, we have conducted ultra-fine scale magnetostratigraphy on a Mn crust sample D96-m4 from northwest Pacific (water depth 1940 m) with a high-resolution SQUID microscope at Vanderbilt University. Various rock-magnetic techniques delineate the presence of well dispersed single domain magnetic mineral with coercivity of about 30

mT and Curie temperature of about 550-570 degree C. However, low temperature measurement did not show Verwey transition characteristic of magnetite and X-ray diffractometry on magnetic separate did not show any peaks of magnetite or maghemite. Two thin sections of 5 mm width x 35 mm length x 0.2 mm thickness were taken from a Mn crust, which are perpendicular to each other. The slices were subjected to SQUID scanning on 85 microns grids with a spatial resolution of about 100 microns for NRM, and after 10 and 20 mT AF demagnetization. The SQUID microscopy revealed fine scale magnetic anomaly parallel to the growth pattern. The identification of polarity boundaries made it possible to estimate growth rate of the Mn crust as 4.5 mm per Myr. The result is much less than the previous estimate on the same Mn crust block[147], however, it is rather consistent with the estimate by 10Be over 9Be (5.9 mm per Myr).[148-152]

MONLITHIC MULTILOOP SQUID MAGNETOMETERS FOR HIGH RESOLUTION SQUID MICROSCOPY

L. E. Fong, K. McBride, J. R. Holzer, M. Radparvar*, F. Baudenbacher

Living State Physics Vanderbilt University

*HYPRES

American Physics Society (APS), Texas

2003 March Meeting

Electric currents or magnetic fields play a key role in a wide range of biological phenomena. In order to image biomagnetic fields and to discriminate between theoretical models, spatial resolutions below 1 mm and field sensitivities below one $pT/Hz^{1/2}$ are required. Previously we have used multiturn miniature cylindrical pickup coils coupled to commercial SQUID sensors. The main drawback is the inefficient coupling of the small coils to the SQUID and the distribution of the sensing volume, which effectively results in a reduction of spatial resolution. Therefore, we have designed Nb thin film multiloop SQUID magnetometers, which have multiple loops arrange in a cart wheel configuration connected in parallel with the SQUID. Three different designs were characterized: 250 μm, 500 μm and 1000 μm pick up loop diameter comprised of 5, 6 and 8 spokes, respectively. With the 250 μm design, we have achieved a field sensitivity of 800 $fT/Hz^{1/2}$ with a flux noise of 6.5 $\mu\Phi_0/Hz^{1/2}$ for frequencies above 1 Hz and a spacing between the sensor and the room temperature sample of 75 μm. In conclusion the

multiloop SQUID allows us not only to achieve higher sensitivities, but also to confine the sensing volume to a plane, which in turn leads to a higher spatial resolution.

MONOLITHIC NIOBIUM-BASED SQUID MAGNOMETERS

FOR HIGH RESOLUTION MAGNETIC FIELD IMAGING

OF ROOM TEMPERATURE SAMPLES

M. Radparvar*, F. Baudenbacher*, _L.E. Fong, J.R. Holzer,

E.A. Lima, K. McBride

Living State Physics Vanderbilt University

*HYPRES

Applied Superconductivity, Washington

2006 Conference

HIGH-RESOLUTION MAGNETIC IMAGING OF ROOM TEMPERATURE SAMPLES USING NIOBIUM THIN-FILM MONOLITHIC SQUIDS INCORPORATED IN A SCANNING MICROSCOPE

L.E. Fong,_J. R. Holzer, K. McBride, M. Radparvar,* F. Baudenbacher

Living State Physics Vanderbilt University

*HYPRES

Applied Superconductivity, Florida

2004 Conference

We have developed niobium thin-film monolithic low-temperature superconducting quantum interference device (SQUID) magnetometers and incorporated them in a scanning microscope. The SQUID microscope is used to image magnetic fields associated with action currents in cardiac and brain tissue, as well as remanent magnetizations of geological samples. Our system allows us to bring a 4.2 K sensor within a distance of less than 100 μm to biological samples at physiological temperatures. In order to cover spatial resolutions from tens of microns to a millimeter with maximum field sensitivity, we have used two different design approaches to optimize the SQUID performance as the size of the sensing area is increased. For a sensing area of less than 150 mm, we used a bare SQUID design and achieved a field sensitivity of 1 $pT/Hz^{1/2}$. For spatial resolutions larger than 150 mm, bare SQUIDs can not be used due to their large inductance. For this scale, we used miniature multiloop SQUIDs with a field sensitivity

of 450 fT/Hz$^{1/2}$ for frequencies >50 Hz. We have conducted paleomagnetic analyses with the bare SQUID and mapped the magnetic fields of action currents on isolated cardiac tissue with the multiloop SQUID design.

COMBINED HIGH RESOLUTION MCG AND ACTION POTENTIAL IMAGING

J.R. Holzer, V. Y. Sidorov, K. McBride, L. Fong_, F. Baudenbacher

Living State Physics Vanderbilt University

Biomagnetism, Massachusetts

2004 Conference

Electric currents or magnetic fields play a key role in a wide range of biological phenomena. In order to image biomagnetic fields and to discriminate between theoretical models spatial resolutions below 1 mm and field sensitivities below one $pT/Hz^{1/2}$ are required. We have developed niobium thin-film monolithic low-temperature superconducting quantum interference device (SQUID) magnetometers and incorporated them in a scanning microscope for imaging biomagnetic fields or remnant magnetizations of geological samples. Our system allows us to bring a 4 K SQUID within a distance of less than 100 μm to biological samples at physiological temperatures. In order to cover spatial resolutions form tens of microns to a mm we have used two different design approaches to optimize the SQUID performance as the size of the sensing area is increased. For a sensing area of less than 150 μm we used a bare SQUID design and achieved a field sensitivity of 1 $pT/Hz^{1/2}$. For spatial resolutions larger than 150 μm bare SQUIDs can not be used due to their large inductance. For the spatial scale between 250 μm and 1 mm we used hand wound miniature pickup coils coupled to commercially available SQUID sensor and monolithic miniature multiloop SQUIDs. For the multiloop

SQUIDs we achieved field sensitivities between 120 fT/ $Hz^{1/2}$ and 450 fT/$Hz^{1/2}$ at frequencies >0.4 Hz for a 1 mm and 250 μm diameter sensor, respectively. We have conducted paleomagnetic analyses with the single loop SQUID and mapped the magnetic fields of action currents in cardiac tissue with the multiloop SQUID.

MONOLITHIC HIGH RESOLUTION SQUID SENSORS FOR IMAGING BIOMAGNETIC FIELDS

L. E. Fong, K.K. McBride, J.R. Holzer, M. Radparvar,* F.J. Baudenbacher

Living State Physics Vanderbilt University

*HYPRES

Biomedical Engineering Society, Tennessee

2003 Annual Fall Meeting

Electric currents or magnetic fields play a key role in a wide range of biological activities such as action, injury and developmental currents. In order to image biomagnetic fields in isolated living tissue or small animal preparation and to discriminate between theoretical models, spatial resolutions below 1 mm and field sensitivities below one $pT/Hz^{1/2}$ are required. Previously we have used miniature cylindrical bobbins coupled to commercial SQUID sensors. The main drawback is the inefficient coupling of the small coils to the SQUID and the distribution of the sensing volume, which effectively results in a reduction of spatial resolution. Therefore, we have designed niobium thin film SQUID sensors to directly measure the magnetic field of biological samples at room temperature. We have designed two types of magnetic sensors: bare and multiloop SQUIDs. The bare SQUID consists of a single square washer. This design gives us a field sensitivity of 700 $fT/Hz^{1/2}$ with a flux noise of 1.2 $\Phi_0/Hz^{1/2}$ for frequencies above 1 KHz. The multiloop SQUID has multiple loops arranged

in a cartwheel configuration connected in parallel with the SQUID. Using this design we have achieved a sensitivity of 250 fT/Hz$^{1/2}$ with a flux noise of 1.7 Φ_0/Hz$^{1/2}$. In conclusion, these monolithic SQUIDs allow us not only to achieve higher sensitivities, but also to confine the sensing volume to a plane, which in turn leads to a higher spatial resolution.

BIBLIOGRAPHY

1. Baudenbacher,F, Peters,NT, Baudenbacher,P, Wikswo,JP. High Resolution Imaging of Biomagnetic Fields Generated by Action Currents in Cardiac Tissue Using a LTS-SQUID Microscope, Physica C, 368, 24-31, 2002

2. Baudenbacher,FJ et al. The Role of Anisotropy on the Initiation and Propagation of Action Currents in Cardiac Tissue. Bull.APS, 46, 1173, 2001

3. Joyner,RW, Westerfield,M, Moore,JW. Effects of Cellular Geometry on Current Flow During a Propagated Action Potential, Biophys. J., 31, 183-194, 1980

4. Fast,VG and Kleber,AG. Cardiac Tissue Geometry As a Determinant of Unidirectional Conduction Block - Assessment of Microscopic Excitation Spread by Optical Mapping in Patterned Cell-Cultures and in a Computer-Model, Cardiovasc. Res., 29, 697-707, 1995

5. Fast,VG and Kleber,AG. Anisotropic Conduction in Monolayers of Neonatal Rat-Heart Cells Cultured on Collagen Substrate, Circ. Res., 75, 591-595, 1994

6. Hunter,PJ, Pullan,AJ, Smaill,BH. Modeling Total Heart Function, Annu. Rev. Biomed. Engr., 5, 147-177, 2003

7. Baudenbacher,F, Peters,NT, Wikswo,JP, Jr. High Resolution Low-Temperature Superconductivity Superconducting Quantum Interference Device Microscope for Imaging Magnetic Fields of Samples at Room Temperatures, Rev. Sci. Instrum., 73, 1247-1254, 2002

8. Baudenbacher,FJ, Peters,NT, Wikswo,JP, Jr., Radparvar,M. High Resolution LTS-SQUID Magnetometer. Bull.APS, 43, 1626, 1998

9. Baudenbacher,FJ, Peters,NT, Baudenbacher,P, Wikswo,JP, Jr. High Resolution Magnetic Imaging of Action Currents in Cardiac Tissue. Bull.APS, 45, 834, 2000

10. Baudenbacher,F, Fong,LE, Holzer,JR, Radparvar,M. Monolithic Low-Transition-Temperature Superconducting Magnetometers for High Resolution Imaging Magnetic Fields of Room Temperature Samples, Appl. Phys. Lett., 82, 3487-3489, 2003

11. Fong,LE, Holzer,JR, McBride,K, Lima,EA, Baudenbacher,F, Radparvar,M. High-Resolution Imaging of Cardiac Biomagnetic Fields Using a Low-Transition-Temperature Superconducting Quantum Interference Device Microscope, Appl. Phys. Lett., 84, 3190-3192, 2004

12. Fong,LE, Holzer,JR, McBride,KK, Lima,EA, Baudenbacher,F, Radparvar,M. High-Resolution Room-Temperature Sample Scanning Superconducting Quantum Interference Device Microscope Configurable for Geological and Biomagnetic Applications, Rev. Sci. Instrum., 76, 053703- 2005

13. Guasp,FT. The Cardiac Muscle. Juan March Foundation, Madrid, 11, 1973

14. Kocica,MJ, Corno,AF, Carreras-Costa,F, Ballester-Rodes,M, Moghbel,MC, Cueva,CNC, Lackovic,V, Kanjuh,VI, Torrent-Guasp,F. The Helical Ventricular Myocardial Band: Global, Three-Dimensional, Functional Architecture of the Ventricular Myocardium, Eur. J. Cardiothorac. Surg., 29, S21-S40, 2006

15. Ross,DN. Torrent-Guasp's Anatomical Legacy, Eur. J. Cardiothorac. Surg., 29, S18-S20, 2006

16. Roth,BJ and Wikswo,JP, Jr. Electrically Silent Magnetic Fields, Biophys. J., 50, 739-745, 1986

17. dos Santos,RW, Kosch,O, Steinhoff,U, Bauer,S, Trahms,L, Koch,H. MCG to ECG Source Differences: Measurements and a 2D Computer Model Study, J. Electrocardiol., 37, Suppl.1, 123-127, 2004

18. Link,A, Endt,P, Oeff,M, Trahms,L. Variability of the QRS Signal in High-Resolution Electrocardiograms and Magnetocardiograms, IEEE Trans. Biomed. Eng., 48, 133-142, 2001

19. SQUID Sensors: Fundamentals, Fabrication and Applications. Weinstock,H, ed. Kluwer Academic Publishers, 1996

20. Dahlberg,ED and Proksch,R. Magnetic Microscopies: the New Additions, J. Magn. Magn. Mater., 200, 720-728, 1999

21. Jenks,WG, Thomas,IM, Wikswo,JP, Jr. SQUIDs. In: Encyclopedia of Applied Physics, Trigg,GL, Vera,ES, Greulich,W, eds. VCH Publishers, Inc., New York, NY, 1996

22. Kirtley,JR. SQUID Microscopy for Fundamental Studies, Physica C: Superconductivity, 368, 55-65, 2002

23. Drung,D. Recent Low-Temperature Squid Developments, IEEE Trans. Appl. Supercond., 4, 121-127, 1994

24. Janawadkar,MP, Baskaran,R, Nagendran,R, Gireesan,K, Harishkumar,N, Saha,R, Vaidhyanathan,LS, Jayapandian,J, Hariharan,Y, Radhakrishnan,TS. SQUID-Based Measuring Systems, Pramana-Journal of Physics, 58, 1159-1164, 2002

25. Fong de los Santos, Luis E., High-resolution imaging of magnetic fields using scanning superconducting quantum interference device (SQUID) microscopy, Ph.D. Dissertation, Vanderbilt University, 2005

26. Fagaly,RL. Superconducting Quantum Interference Device Instruments and Applications, Rev. Sci. Instrum., 77, 101101-101145, 2006

27. Gruhl,F, Muck,M, von Kreutzbruck,M, Dechert,J. A Scanning Superconducting Quantum Interference Device Microscope With High Spatial Resolution for Room Temperature Samples, Rev. Sci. Instrum., 72, 2090-2096, 2001

28. Jenks,WG, Ma,YP, Parente Ribeiro,E, Wikswo,JP. SQUID NDE of Composite Materials With Magnetic Tracers, (unpublished), 1997

29. Jenks,WG, Sadeghi,SSH, Wikswo,JP, Jr. SQUIDs for Nondestructive Evaluation, J. Phys. D: Appl. Phys., 30, 293-323, 1997

30. Kirtley,JR and Wikswo,JP, Jr. Scanning SQUID Microscopy, Annual Review of Materials Science, 29, 117-148, 1999

31. Clarke,J, Goubau,WM, Ketchen,MB. Tunnel Junction Dc Squid - Fabrication, Operation, and Performance, J. Low Temp. Phys., 25, 99-144, 1976

32. Bishop,DJ. Flux Lattice Melting, Science, 273, 1811-1811, 1996

33. Kleiner,R, Koelle,D, Ludwig,F, Clarke,J. Superconducting Quantum Interference Devices: State of the Art and Applications, Proc. IEEE, 92, 1534-1548, 2004

34. Landau,LD. Collected Papers of L.D. Landau. New York, Gordon and Breach, 1965

35. Ginzburg,VL and Landau,LD. On the Theory of Superconductivity, J. Exp. Theor. Phys. (U. S. S. R.), 20, 1064-1082, 1950

36. Meissner,W and Ochsenfeld,R. A New Effect in Penetration of Superconductors, Die Naturwissenschaften, 21, 787-788, 1933

37. Josephson,BD. The Discovery of Tunneling Supercurrents, Science, 184, 527-530, 1974

38. Shapiro,S. Josephson Currents in Superconducting Tunneling; the Effect of Microwaves and Other Observations, Phys. Rev. Lett., 11, 80-82, 1963

39. Tinkham,M. Introduction. In: Group theory and quantum mechanics, McGraw-Hill, New York, 1-5, 1964

40. Drung,D. DC SQUID Systems Overview, Superconductor Science and Technology, 4, 377-385, 1991

41. Bertolini,L. The US Particle Accelerator School Cryosorption Pumps. Lawrence Livermore National Laboratory, 2002

42. Leybold Vacuum Products and Reference Book: Cryopumps, Cryogenics. 2001

43. Wikswo,JP, Jr., Ma,YP, Sepulveda,NG, Staton,DJ, Tan,S, Thomas,IM. Superconducting Magnetometry: A Possible Technique for Aircraft NDE, Proc. SPIE, 2001, 164-190, 1993

44. Black,RC, Mathai,A, Wellstood,FC, Dantsker,E, Miklich,AH, Nemeth,DT, Kingston,JJ, Clarke,J. Magnetic Microscopy Using a Liquid Nitrogen Colled $YBa_2Cu_3O_7$ Superconducting Quantum Interference Device, Appl. Phys. Lett., 62, 2128-2830, 1993

45. Chatraphorn,S, Fleet,EF, Wellstood,FC, Knauss,LA. Noise and Spatial Resolution in SQUID Microscopy, IEEE Trans. Appl. Supercond., 11, 234-237, 2001

46. Dechert,J, Mueck,M, Heiden,C. A Scanning SQUID Microscope for Samples at Room Temperature, IEEE Trans. Appl. Supercond., 9, 4111-4114, 1999

47. Black,RC, Wellstood,FC, Dantsker,E, Miklich,AH, Nemeth,DT, Koelle,D, Ludwig,F, Clarke,J. Microwave Microscopy Using a Superconducting Quantum Interference Device, Appl. Phys. Lett., 66, 99-101, 1995

48. Fleet,E, Gilbertson,A, Chatraphorn,S, Tralshawala,N, Weinstock,H, Wellstood,FC. Imaging Defects in Cu-Clad NbTi Wire Using a High-T-c Scanning SQUID Microscope, IEEE Trans. Appl. Supercond., 11, 215-218, 2001

49. Gallop,J. SQUIDs: Some Limits to Measurement, Superconductor Science and Technology, 16, 1575-1582, 2003

50. Aubon,CR and Peters,NR. Miniature Long-Life Tactical Stirling Cryocoolers for Volume Production, Superconductor Industry, 13-22, 1996

51. Beckett,CD, Lauhala,VC, Neely,R, Penswick,LB, Ritter,DC, Nelson,RL, Wimer,BP, Flexure Bearing Support, With Particular Application to Stirling Machines, Patent Number - 5522214, 1996

52. He,Y, Ding,H, Yan,X, Zhang,F, Han,S, Dong,S, Chen,G, Jin,D. Development of Scanning SQUID Microscope for Studying Room Temperature Samples, Physica B: Condensed Matter, 329-333, 1508-1509, 2003

53. Ketchen,MB. Design Considerations for Dc Squids Fabricated in Deep Submicron Technology, IEEE Trans. Magn., 27, 2916-2919, 1991

54. Jaycox,JM and Ketchen,MB. Planar Coupling Scheme for Ultra Low-Noise Dc Squids, IEEE Trans. Magn., 17, 400-403, 1981

55. Bork,J, Hahlbohm,H-D, Klein,R, Schnabel,A. The 8-Layered Magnetically Shielded Room of the PTB: Design and Construction. In: Biomag2000, Proc. 12th Int. Conf. on Biomagnetism, Nenonen,J, Ilmoniemi,RJ, Katila,T, eds. Helsinki Univ. of Technology, Espoo, Finland, 970-973, 2001

56. Heinonen,P, Tuomola,M, Lekkala,J, Malmivuo,JAV. Properties of a Thick-Walled Conducting Enclosure in Low-Frequency Magnetic Shielding, Journal of Physics E: Instrumentation, 13, 569-570, 1980

57. Hirschkoff,EC, Magnetically Shielded Enclosure, Patent Number - 5,081,071, 1992

58. Kajiwara,G, Harakawa,K, Ogata,H. High-Performance Magnetically Shielded Room, IEEE Trans. Magn., 32, 2582-2585, 1996

59. Barach,JP, Freeman,JA, Wikswo,JP, Jr. Experiments on the Magnetic Field of Nerve Action Potentials, J. Appl. Phys., 51, 4532-4538, 1980

60. Correa,JS, Eckhause,TA, Gwinn,EG, Thomas,M. Temperature Dependence of Critical Currents in Nb/InAs/Nb Josephson Junction Arrays, Physica E: Low-Dimensional Systems and Nanostructures, 12, 927-930, 2002

61. Ketchen,MB, Bhushan,M, Kaplan,SB, Gallagher,WJ. Low-Noise Dc Squids Fabricated in Nb-Al2O3-Nb Trilayer Technology, IEEE Trans. Magn., 27, 3005-3008, 1991

62. Drung,D, Knappe,S, Koch,H. Theory For The Multiloop Dc Superconducting Quantum Interference Device Magnetometer And Experimental-Verification, J. Appl. Phys., 77, 4088-4098, 1995

63. Stewart,WC. Current-Voltage Characteristics of Josephson Junctions, Appl. Phys. Lett., 12, 277-280, 1968

64. McCumber,DE. Effect of Ac Impedance on Dc Voltage-Current Characteristics of Superconductor Weak-Link Junctions, J. Appl. Phys., 39, 3113-3118, 1968

65. Tesche,CD and Clarke,J. Dc Squid - Noise and Optimization, J. Low Temp. Phys., 29, 301-331, 1977

66. Jenks,WG, Thomas,IM, Wikswo,JP, Jr. SQUIDs. In: Encyclopedia of Applied Physics: Sonoluminescence to Steel, Trigg,GL, Vera,ES, Greulich,W, eds. VCH Publishers, Inc., New York, 457-469, 1997

67. Falferi,P, Bonaldi,M, Cerdonio,M, M+,M, Vinante,A, Mezzena,R, Prodi,GA, Vitale,S. Characterization of the Input Noise Sources of a Dc SQUID, J. Low Temp. Phys., V123, 275-302, 2001

68. Koch,RH, Clarke,J, Goubau,WM, Martinis,JM, Pegrum,CM, Vanharlingen,DJ. Flicker (1/F) Noise in Tunnel Junction Dc Squids, J. Low Temp. Phys., 51, 207-226, 1983

69. Rogers,CT and Buhrman,RA. Composition of 1/f Noise in Metal-Insulator-Metal Tunnel Junctions, Phys. Rev. Lett., 53, 1272-1275, 1984

70. Foglietti,V, Gallagher,WJ, Ketchen,MB, Kleinsasser,AW, Koch,RH, Raider,SI, Sandstrom,RL. Low-Frequency Noise in Low 1/f Noise Dc SQUID's, Appl. Phys. Lett., 49, 1393-1395, 1986

71. Koch,RH, Clarke,J, Martinis,JM, Goubau,WM, Pegrum,CM, Vanharlingen,DJ. Investigation of 1/F Noise in Tunnel Junction Dc Squids, IEEE Trans. Magn., 19, 449-452, 1983

72. Plonsey,R et al. Bioelectricity: a Quantitative Approach. Kluwer Academic/Plenum Publishers, New York, 2000

73. Hooks,DA, Tomlinson,KA, Marsden,SG, LeGrice,IJ, Smaill,BH, Pullan,AJ, Hunter,PJ. Cardiac Microstructure: Implications for Electrical Propagation and Defibrillation in the Heart, Circ. Res., 91, 331-338, 2002

74. Colli-Franzone,P, Guerri,L, Pennacchio,M, Taccardi,B. Spread of Excitation in 3-D Models of the Anisotropic Cardiac Tissue. III. Effects of Ventricular Geometry and Fiber Structure on the Potential Distribution, Math. Biosci., 151, 51-98, 1998

75. Roth,BJ, Guo,W-Q, Wikswo,JP, Jr. The Effects of Spiral Anisotropy on the Electric Potential and the Magnetic Field at the Apex of the Heart, Math. Biosci., 88, 191-221, 1988

76. Hooks,DA, LeGrice,IJ, Harvey,JD, Smaill,BH. Intramural Multisite Recording of Transmembrane Potential in the Heart, Biophys. J., 81, 2671-2680, 2001

77. Najafi,K, Ji,J, Wise,KD. Scaling Limitations of Silicon Multichannel Recording Probes, IEEE Trans. Biomed. Eng., 37, No.1, 1-11, 1990

78. Koudelka-Hep,M and van der Wal,PD. Microelectrode Sensors for Biomedical and Environmental Applications, Electrochim. Acta, 45, 2437-2441, 2000

79. Janse,MJ, van Capelle,FJL, Freud,GE, Durrer,D. Circus Movement Within the AV Node As a Basis for Supraventricular Tachycardia As Shown by Multiple Microelectrode Recording in the Isolated Rabbit Heart, Circ. Res., XXVIII, 403-414, 1971

80. Roth,BJ and Wikswo,JP, Jr. The Magnetic Field of a Single Axon: A Comparison of Theory and Experiment, Biophys. J., 48, 93-109, 1985

81. Sase,I, Miyata,H, Corrie,JET, Craik,JS, Kinosita,K, Jr. Real Time Imaging of Single Fluorophores on Moving Actin With an Epifluorescence Microscope, Biophys. J., 69, 323-328, 1995

82. Lin,S-F, Abbas,RA, Wikswo,JP, Jr. High-Resolution High-Speed Synchronous Epifluorescence Imaging of Cardiac Activation, Rev. Sci. Instrum., 68, 213-217, 1997

83. Hernandez,H, Hwang,GS, Lin,SF. Synchronization of Ventricular Fibrillation With Electrical Pacing Guided by Optical Signals: Comparison of Pacing Locations. Photonic Therapeutics and Diagnostics II, Proceedings of SPIE, 6078, Article No.- 60782O 2006

84. Lin,S-F, Qian,Y-W, Sung,RJ. Effects of Intravenous Amiodarone on Ventricular Vulnerability: An Optical Imaging Study in Isolated Rabbit Hearts. J.Am.Coll.Cardiol., 31, 279A, 1998

85. Lin,S-F and Wikswo,JP, Jr. 3-D Measurement and Visualization of Electrical Propagation on Heart Studies. Bull.APS, 42, 1799, 1997

86. Roth, Bradley J., The Magnetic Field of a Single Axon: A Comparison of Theory and Experiment, M.S. (non-thesis), Vanderbilt University, 1985

87. Roth,BJ and Wikswo,JP, Jr. The Electrical Potential and the Magnetic Field of an Axon in a Nerve Bundle, Math. Biosci., 76, 37-57, 1985

88. Baudenbacher,FJ, Peters,NT, Baudenbacher,P, Wikswo,JP, Jr. High Resolution Imaging of Biomagnetic Fields Generated by Action Currents in Cardiac Tissue Using a LTS-SQUID Microscope, Physica C, 368, 24-31, 2002

89. Holzer,JR, Fong,LE, Sidorov,VY, Wikswo,JP, Jr., Baudenbacher,F. High Resolution Magnetic Images of Planar Wave Fronts Reveal Bidomain Properties of Cardiac Tissue, Biophys. J., 87, 4326-4332, 2004

90. Streeter,DD. Gross Morphology and Fiber Geometry of the Heart. In: The Cardiovascular System, Berne,RM, Sperelakis,N, Geigert,SR, eds. American Physiological Society Press, Bethesda, 61-122, 1979

91. Fischer,G, Tilg,B, Modre,R, Huiskamp,GJM, Fetzer,J, Rucker,W, Wach,P. A Bidomain Model Based BEM-FEM Coupling Formulation for Anisotropic Cardiac Tissue, Ann. Biomed. Eng., 28, 1229-1243, 2000

92. Ohyu,S, Okamoto,Y, Kuriki,S. Use of the Ventricular Propagated Excitation Model in the Magnetocardiographic Inverse Problem for Reconstruction of Electrophysiological Properties, IEEE Trans. Biomed. Eng., 49, 509-519, 2002

93. Uchida,S, Iramina,K, Goto,K, Ueno,S. High Resolution Magnetocardiography for the Study of Dynamic Propagation of Excitation Sites in Rat Cardiac Muscles, IEEE Trans. Magn., 35, 4124-4126, 1999

94. Roth,BJ and Beaudoin,DL. Approximate Analytical Solutions of the Bidomain Equations for Electrical Stimulation of Cardiac Tissue With Curving Fibers, Phys. Rev. E, 67, 051925- 2003

95. Staton,DJ, Friedman,RN, Wikswo,JP, Jr. High Resolution SQUID Magnetocardiographic Mapping of Action Currents in Canine Cardiac Slices. Circulation, 84, II-667, 1991

96. Koch,H. SQUID Magnetocardiography: Status and Perspectives, IEEE Trans. Appl. Supercond., 11, 49-59, 2001

97. Koch,H and Haberkorn,W. Magnetic Field Mapping of Cardiac Electrophysiological Function, Philos. Trans. R. Soc. London A, 359, 1287-1298, 2001

98. Barach,JP. A Simulation of Cardiac Action Currents Having Curl, IEEE Trans. Biomed. Eng., 40, 49-58, 1993

99. Sidorov,VY, Woods,MC, Baudenbacher,P, Baudenbacher,F. Examination of Stimulation Mechanism and Strength-Interval Curve in Cardiac Tissue, Am. J. Physiol. Heart, 289, H2602-H2615, 2005

100. Woods,MC. Field Stimulation of the Diastolic Rabbit Heart: The Role of Shock Strength and Duration on Epicardial Activation and Propagation. In: The response of the cardiac bidomain of electrical stimulation, PhD Dissertation, Vanderbilt University, 109-138, 2005

101. Roth,BJ. Action Potential Propagation in a Thick Strand of Cardiac Muscle.1990

102. Beeler,GW and Reuter,H. Reconstruction of the Action Potential of Ventricular Myocardial Fibers, J. Physiol., 268, 177-210, 1977

103. Weinstock,H. SQUID Sensors: Fundamentals, Fabrication and Applications. Weinstock,H, ed. Kluwer Academic, Boston, 1996

104. Thomas,IM, Freake,SM, Swithenby,SJ, Wikswo,JP, Jr. A Distributed Quasi-Static Ionic Current Source in the 3-4 Day Old Chicken Embryo, Phys. Med. Biol., 38, 1311-1328, 1993

105. Chemla,YR, Grossman,HL, Lee,TS, Clarke,J, Adamkiewicz,M, Buchanan,BB. A New Investigation of Bacterial Motion: Superconducting Quantum Interference Device Microscopy of Magnetotactic Bacteria, Biophys. J., 76, 3323-3330, 1999

106. Holzer,JR, Fong,LE, Sidorov,VY, Wikswo,JP, Jr., Baudenbacher,F. High Resolution Magnetic Images of Planar Wave Fronts Reveal Bidomain Properties of Cardiac Tissue, Biophys. J., 87, 4326-4332, 2004

107. Baudenbacher,F, Fong,LE, Thiel,G, Wacke,M, Jazbinsek,V, Holzer,JR, Stampfl,A, Trontelj,Z. Intracellular Axial Current in Chara Corallina Reflects the Altered Kinetics of Ions in Cytoplasm Under the Influence of Light, Biophys. J., 88, 690-697, 2005

108. Chatraphorn,S, Fleet,EF, Wellstood,FC, Knauss,LA, Eiles,TM. Scanning SQUID Microscopy of Integrated Circuits, Appl. Phys. Lett., 76, 2304-2306, 2000

109. Fleet,EF, Chatraphorn,S, Wellstood,FC, Knauss,LA. HTS Scanning SQUID Microscopy of Active Circuits, IEEE Trans. Appl. Supercond., 9, 4103-4106, 1999

110. Weinstock,H. A Review of SQUID Magnetometry Applied to Nondistructive Evaluation, IEEE Trans. Magn., 27, 3231-3236, 1991

111. Klein,U, Walker,ME, Carr,C, McKirdy,DM, Pegrum,CM, Donaldson,GB, Cochran,A, Nakane,H. Integrated Low-Temperature Superconductor SQUID Gradiometers for Nondestructive Evaluation, IEEE Trans. Appl. Supercond., 7, 3037-3039, 1997

112. Abedi,A, Fellenstein,J, Lucas,AJ, Wikswo,JP, Jr. A Superconducting Quantum Interference Device Magnetometer System for Quantitative Analysis and Imaging of Hidden Corrosion Activity in Aircraft Aluminum Structures, Rev. Sci. Instrum., 70, 4640-4651, 1999

113. Weiss,BP, Vali,H, Baudenbacher,FJ, Kirschvink,JL, Stewart,ST, Shuster,DL. Records of an Ancient Martian Magnetic Field in ALH84001, Earth and Planetary Science Letters, 201, 449-463, 2002

114. Weiss,BP, Kirschvink,JL, Baudenbacher,FJ, Vali,H, Peters,NT, Macdonald,FA, Wikswo,JP. A Low Temperature Transfer of ALH84001 From Mars to Earth, Science, 290, 791-795, 2000

115. Roth,BJ, Sepulveda,NG, Wikswo,JP, Jr. Using a Magnetometer to Image a Two-Dimensional Current Distribution, J. Appl. Phys., 65, 361-372, 1989

116. Baudenbacher,F, Peters,NT, Wikswo,JP, Jr. High Resolution Low-Temperature Superconductivity Superconducting Quantum Interference Device Microscope for Imaging Magnetic Fields of Samples at Room Temperatures, Rev. Sci. Instrum., 73, 1247-1254, 2002

117. Weiss,BP, Baudenbacher,FJ, Wikswo,JP, Kirschvink J.L. Magnetic Microscopy Promises a Leap in Sensitivity and Resolution, Eos Trans. AGU, 82, 513-518, 2001

118. Tesche,CD and Clarke,J. Dc Squid - Noise and Optimization, J. Low Temp. Phys., 29, 301-331, 1977

119. Jaycox,JM and Ketchen,MB. Planar Coupling Scheme for Ultra Low-Noise Dc Squids, IEEE Trans. Mag., 17, 400-403, 1981

120. Zimmerman,JE. Sensitivity Enhancement Of Superconducting Quantum Interference Devices Through Use Of Fractional-Turn Loops, J. Appl. Phys., 42, 4483-4487, 1971

121. Fong,LE, Holzer,JR, McBride,K, Lima,EA, Baudenbacher,F, Radparvar,M. High-Resolution Imaging of Cardiac Biomagnetic Fields Using a Low-Transition-Temperature Superconducting Quantum Interference Device Microscope, Appl. Phys. Lett., 84, 3190-3192, 2004

122. Lee,TS, Dantsker,E, Clarke,J. High-Transition Temperature Superconducting Quantum Interference Device Microscope, Rev. Sci. Instrum., 67, 4208-4215, 1996

123. Gruhl,F, Muck,M, von Kreutzbruck,M, Dechert,J. A Scanning Superconducting Quantum Interference Device Microscope With High Spatial Resolution for Room Temperature Samples, Rev. Sci. Instrum., 72, 2090-2096, 2001

124. Black R.C., Magnetic Microscopy using a Superconducting Quantum Interference Device, PhD, University of Maryland, 1995

125. Clarke,J, Goubau,WM, Ketchen,MB. Tunnel Junction Dc Squid - Fabrication, Operation, and Performance, J. Low Temp. Phys., 25, 99-144, 1976

126. Kirschvink J.L. How Sensitivite Should a Rock Magnetometer Be for Use in Paleomagnetism? In: SQUID Applications to Geophysics, Weinstock,H and Overton W.C., eds. 111-114, 1981

127. Weiss,BP, Vali,H, Baudenbacher,FJ, Kirschvink,JL, Stewart,ST, Shuster,DL. Records of an Ancient Martian Magnetic Field in ALH84001, Earth and Planetary Science Letters, 201, 449-463, 2002

128. Weiss,BP, Kirschvink,JL, Baudenbacher,FJ, Vali,H, Peters,NT, Macdonald,FA, Wikswo,JP. A Low Temperature Transfer of ALH84001 From Mars to Earth, Science, 290, 791-795, 2000

129. Wikswo,JP, Jr. Applications of SQUID Magnetometers to Biomagnetism and Nondestructive Evaluation. In: Applications of Superconductivity, Weinstock,H, ed. Kluwer Academic Publishers, Netherlands, 139-228, 2000

130. Langrill,DM and Roth,BJ. The Effect of Plunge Electrodes During Electrical Stimulation of Cardiac Tissue, IEEE Trans. Biomed. Eng., 48, 1207-1211, 2001

131. Lin,S-F, Abbas,RA, Wikswo,JP, Jr. High-Resolution High-Speed Synchronous Epifluorescence Imaging of Cardiac Activation, Rev. Sci. Instrum., 68, 213-217, 1997

132. Holzer J.R., Fong L.E., Sidorov V.Y., Wikswo J.P., Baudenbacher F. Magnetic and Fluorescent Imaging of Plane Waves in Cardiac Tissue Reveals Currents Parallel to the Wave Front, Accepted to Biophysical Journal, 2004

133. Plonsey,R and Barr,RC. Current Flow Patterns in Two-Dimensional Anisotropic Bisyncytia With Normal and Extreme Conductivities, Biophys. J., 45, 557-571, 1984

134. Plonsey,R and Rudy,Y. Electrocardiogram Sources in a 2-Dimensional Anisotropic Activation Model, Med. Biol. Eng. Comp., 18, 87-94, 1980

135. Wikswo,JP, Jr. High-Resolution Magnetic Imaging: Cellular Action Currents and Other Applications. In: SQUID Sensors: Fundamentals, Fabrication and Applications, Weinstock,H, ed. Kluwer Academic Publishers, The Netherlands, 307-360, 1996

136. Drung,D, Cantor,R, Peters,M, Ryhanen,T, Koch,H. Integrated Dc Squid Magnetometer With High Dv/Db, IEEE Trans. Mag., 27, 3001-3004, 1991

137. Drung,D, Zimmermann,R, Cantor,R, Erne,SN, Koch,H, Matthies,KP, Peters,M, Scheer,HJ, Stollfuss,D. A 37-Channel Dc-Squid Magnetometer System, Clin. Phys. Physiol. Meas., 12, 21-29, 1991

138. Casey,A, Cowan,B, Digby,M, Dyball,H, Korber,R, Li,J, Lusher,C, Maidanov,V, Nyeki,J, Saunders,J et al. Nuclear Magnetic Resonance Using DC SQUIDs With APF, Physica C-Superconductivity and Its Applications, 399, 93-97, 2003

139. Drung,D. High-Performance DC SQUID Read-Out Electronics, Physica C-Superconductivity and Its Applications, 368, 134-140, 2002

140. Drung,D, Knappe,S, Koch,H. Theory for the Multiloop Dc Superconducting Quantum Interference Device Magnetometer and Experimental-Verification, J. Appl. Phys., 77, 4088-4098, 1995

141. Moya,A, Baudenbacher,FJ, Wikswo,JP, Jr., Wellstood,FC. Design of High Resolution HTS-SQUID Magnetometers for Biomagnetic Imaging, IEEE Trans. Appl. Supercond., 9, 3511-3514, 1999

142. Koch,RH, Clarke,J, Goubau,WM, Martinis,JM, Pegrum,CM, Vanharlingen,DJ. Flicker (1/F) Noise in Tunnel Junction Dc Squids, J. Low Temp. Phys., 51, 207-226, 1983

143. Rogers,CT and Buhrman,RA. Conductance Fluctuations and Low-Frequency Noise in Josephson-Junctions, IEEE Trans. Mag., 19, 453-457, 1983

144. Roth,BJ and Wikswo,JP, Jr. A Bidomain Model for the Extracellular Potential and Magnetic Field of Cardiac Tissue, IEEE Trans. Biomed. Eng., BME-33, 467-469, 1986

145. Henriquez,CS. Simulating the Electrical Behavior of Cardiac Tissue Using the Bidomain Model, Crit. Rev. Biomed. Eng., 21, 1-77, 1993

146. Roth,BJ and Woods,MC. The Magnetic Field Associated With a Plane Wave Front Propagating Through Cardiac Tissue, IEEE Trans. Biomed. Eng., 46, 1288-1292, 1999

147. Joshima,M and Usui,A. Magnetostratigraphy of Hydrogenetic Manganese Crusts From Northwestern Pacific Seamounts, Marine Geology, 146, 53-62, 1998

148. Tauxe,L. Sedimentary Records of Relative Paleointensity of the Geomagnetic-Field - Theory and Practice, Reviews of Geophysics, 31, 319-354, 1993

149. Yamazaki,T and Oda,H. A Geomagnetic Paleointensity Stack Between 0.8 and 3.0 Ma From Equatorial Pacific Sediment Cores, Geochemistry Geophysics Geosystems, 6, Article Q11H20,- 2005

150. Yamazaki,T and Oda,H. Orbital Influence on Earth's Magnetic Field: 100,000-Year Periodicity in Inclination, Science, 295, 2435-2438, 2002

151. Oda,H, Nakamura,K, Ikehara,K, Nakano,T, Nishimura,M, Khlystov,O. Paleomagnetic Record From Academician Ridge, Lake Baikal: a Reversal Excursion at the Base of Marine Oxygen Isotope Stage 6, Earth and Planetary Science Letters, 202, 117-132, 2002

152. Oda,H, Shibuya,H, Hsu,V. Palaeomagnetic Records of the Brunhes/Matuyama Polarity Transition From ODP Leg 124 (Celebes and Sulu Seas), Geophys. J. Int., 142, 319-338, 2000